A Study of Particle Identification with the Super-Kamiokande Detector

A Thesis Presented

by

Karl Florian Goebel

to

The Graduate School

in Partial Fulfillment of the Requirements

for the Degree of

Master of Arts

in

Physics

State University of New York
at
Stony Brook

December 1996

State University of New York
at Stony Brook

The Graduate School

Karl Florian Goebel

We, the thesis committee for the above candidate for the Master of Arts degree, hereby recommend acceptance of the thesis.

Professor Chiaki Yanagisawa
Department of Physics

Professor Chang Kee Jung
Department of Physics

Professor George Sterman
Department of Physics

This thesis is accepted by the Graduate School.

Graduate School

Abstract of the Thesis

A Study of Particle Identification with the Super-Kamiokande Detector

by

Karl Florian Goebel

Master of Arts

in

Physics

State University of New York at Stony Brook

1996

A particle identification algorithm has been developed for the study of atmospheric neutrinos with the Super-Kamiokande detector. Preliminary results are obtained for identifying electrons and muons based on a study with a sample of Monte Carlo events. The identification efficiency for particles in a visible energy range 100 MeV to 2 GeV is better than 93% for electrons and 91% for muons. A preliminary analysis with a selected data sample shows results qualitatively consistent with the Monte Carlo study.

Contents

List of Figures

List of Tables

Acknowledgements

First, I would like to thank the German-American Fulbright Commission which made my stay in Stony Brook possible. Here, I had the opportunity to work in an active research group in high energy physics which was a totally new experience for me.

The Super-Kamiokande experiment is a product of many people and my work would not have been possible without their contributions. However, some people deserve special mention. First, I thank my advisor Prof. Chiaki Yanagisawa who guided me during this past academic year and whose support was not limited to the field of physics. I also owe many thanks to Prof. Chang Kee Jung for advise mainly during our weekly meetings.

Much of what I know about computers I learned from my fellow graduate students Brett Viren and Eric Sharkey. I am thankful to Clark McGrew who shared his broad knowledge and experience with me and provided me with many ideas. While writing my thesis I got much support from Jim Hill who revised my first drafts. Through many discussions he help me broaden my

understanding of the physics in Super-Kamiokande. I am grateful to Friedrich König for reviewing the initial drafts of my thesis.

Beyond physics, my stay was enriched by many friends here in Stony Brook. Far from home I received continuous support from my family. Their regular correspondence, however, never made me feel home was far away.

Chapter 1

Introduction

1.1 Theoretical Background

For almost 20 years the "Standard Model" of elementary particle physics which comprises quantum chromodynamics and the Glashow-Weinberg-Salam theory of electroweak processes has been accepted as the theory describing all elementary interactions except gravity. So far there have been no compelling experimental findings requiring a modification of the current Standard Model. However, there is some reason to believe that there is physics beyond the Standard Model.

Particle interactions are very successfully described in terms of local gauge symmetries. In the Standard Model the three fundamental forces reflect three independent symmetries. It seems natural to develop theories where these separate symmetries are part of one larger gauge symmetry.

From a theoretical point of view these grand unified theories (GUTs) are much more satisfying than the Standard Model.

Certainly one of the most exciting phenomena predicted by GUTs is proton decay. In the Standard Model the proton is stable as it is the lightest baryon. It cannot decay into leptons because baryon number is assumed to be conserved. However there is no underlying symmetry that requires baryon and lepton number conservation. In fact most GUTs provide for baryon-lepton interactions.

In the framework of grand unified theories neutrinos are usually put in a large multiplet together with quarks as well as charged leptons [1]. As neutrinos are treated equally with charged leptons and quarks it is natural to assume that they are also massive particles. In analogy to quarks, massive neutrinos can also have flavor mixing. This leads to the possibility of the interesting phenomenon of neutrino oscillations where neutrinos change their flavor state. An observation of neutrino oscillations represents an unambiguous evidence for non standard physics. The existence of neutrino mass is also of importance in Cosmology. Because of the large number of neutrinos expected in the universe, massive neutrinos might considerably contribute to the dark mass. This would have a great impact on the cosmological model of the universe.

1.2 Super-Kamiokande, a Multipurpose Detector

Super-Kamiokande is a 50,000 ton Water Čerenkov Detector in the Kamioka mine in Japan. It detects relativistic charged particles by the Čerenkov light they emit. The detector is located under 1000 meters of mountain rock, which can only be penetrated by neutrinos and very energetic cosmic ray muons. Construction has been completed and data taking started on April 1st, 1996.

Super-Kamiokande is suitable to search for many interesting phenomena in physics [2]. Solar neutrinos produced by nuclear chain-reactions in the core of the sun are within the sensitivity range of the detector [4]. Also, in the case of a nearby supernova explosion the corresponding neutrino burst can be detected. The particle identification program presented in this work is mainly developed for the analysis of atmospheric neutrinos. However, it is also relevant to the analysis of proton decay.

Proton Decay

As mentioned in the previous section proton decay is an unambiguous sign for new physics. If a proton decays inside the detector, charged leptons or mesons are created either directly or as secondary decay products. These

decay products can be detected as their kinetic energy is usually enough to radiate Čerenkov light.

There are many decay modes predicted by different grand unified theories. Particle identification can be used as a tool to identify these decay modes. In 5 years of detector lifetime the exposure will be 110 kiloton-years. This corresponds to a sensitivity to a lifetime of $\sim 10^{33} \sim 10^{34}$ years for most predicted decay modes.

Atmospheric Neutrinos

Originally considered as a background to proton decay measurements, atmospheric neutrinos have attracted much attention because of disagreements between measured and predicted fluxes. Studies mainly focused on the flux ratio $(\nu_\mu + \overline{\nu}_\mu)/(\nu_e + \overline{\nu}_e)$ which was measured to be smaller than predicted by Monte Carlo studies [3]. A favored explanation for this deficit is neutrino oscillation. The study of atmospheric neutrinos might therefore lead to the discovery of non-standard physics. Improved measurements of energy and direction dependence of the ν_μ and ν_e flux will help to clarify this situation.

Atmospheric neutrinos are generated by interactions of cosmic rays with the atmosphere. Primary cosmic rays create secondary particles which decay and thereby emit neutrinos. The energy spans from 10's of MeV to over

10's of TeV. These neutrinos travel 10 km to 10,000 km before reaching the detector where a small fraction interacts with the water in the tank. Highly energetic leptons and mesons created in these interactions are detected.

Super-Kamiokande is designed to measure energy, direction and position of the production vertex of these interaction products. On a statistical basis, this allows one to infer the original neutrino momentum. Also, at some level, ν_μ and ν_e interactions can be distinguished. This reconstruction analysis is the main subject of this thesis.

1.3 Historic Overview and Comparison with other Experiments

The first detectors for atmospheric neutrinos have been built in the 1960's. Using scintillators and flash tubes they detected events induced by neutrinos in the surrounding rock. Highly energetic $\nu_\mu(\overline{\nu_\mu})'s$ ($\langle E_\nu \rangle \approx 100GeV$) create muons that penetrate the detectors. Since the penetration depth of electrons is much shorter, this technique does not work for $\nu_e(\overline{\nu_e})'s$.

In the 1980's several massive detectors were designed to search for proton decay. All of them were deep underground to shield them from cosmic rays. They were searching for events originating inside of the detector. Since ν interactions create the same class of events these detectors also began to

study atmospheric neutrinos.

Two different detector types were developed. The NUSEX and the Frèjus experiments use fine-grained tracking calorimeters [5, 6]. The 150 ton NUSEX detector, located at a depth of 5000 meter water equivalent (m.w.e.) in the Mont Blanc tunnel, consists of 134 1cm thick iron plates interleaved with streamer tubes. Frèjus (4850 m.w.e.) uses 900 tons iron as the primary sensitive mass. The tracks are detected by flash-chamber and Geiger-tube planes. Both detectors provide two orthogonal images of an event but no dE/dx information is available.

The two water Čerenkov detectors IMB and Kamiokande are similar to Super-Kamiokande. IMB [7] consisted of an 8 kton water tank (18 m $\times$ 17 m $\times$ 22.5 m) in the Morton Salt mine, Ohio, USA (1570 m.w.e.), and started taking data in 1982. Only in its final stage starting in 1986 the detector had sufficient light collection efficiency to allow for particle identification. In this stage 2048 20-cm photomultipliers with wavelength shifter plates were installed on all six surfaces pointing inwards. With a coverage of 4%, it monitored the ring pattern of the Čerenkov light emitted by relativistic charged particles. Operating at a trigger threshold of 15 MeV electrons from muon decay (maximum 53 MeV) were detected with a probability of about 80%, which was used to identify the presence of a muon in an event. Particle identification analyzing the difference between ring patterns produced by electrons

Exp.	Data		MC		$(\mu/e)_{data}$
	e-like	μ-like	e-like	μ-like	$(\mu/e)_{MC}$
NUSEX	18	32	20.5	36.8	$0.99^{+0.35}_{-0.25}\pm$ small
Frejus	57	108	70.6	125.8	$1.06^{+0.19}_{-0.16} \pm 0.15$
IMB-3	325	182	257.3	268.0	$0.54 \pm 0.05 \pm 0.12$
Kamiokande	159	151	164.9	260.6	$0.60^{+0.07}_{-0.06} \pm 0.05$
Combined					$0.630 \pm 0.04(stat)$

Table 1.1: Atmospheric neutrino data from the 4 experiments (from [3]).

and muons was 92% efficient.

Kamiokande [8] is a 4.5-kton cylindrical water Čerenkov detector (16 m $\times$ 19 mϕ) in the Kamioka mine 2700 m.w.e. underground. There are 948 50-cm phototubes installed that provide a 20% photocathode coverage. Up to 98% efficiency of particle identification was achieved by this experiment. A 1.5 m thick anticoincidence detector surrounding the inner detector is used to veto entering events which are mainly cosmic ray muons.

The total atmospheric neutrino flux measured by the four experiments described above is lower than the predicted values. However, since the uncertainty in the predicted event rate is approximately $\pm$30%, interest has mainly focused on the ratio $(\nu_\mu + \overline{\nu}_\mu)/(\nu_e + \overline{\nu}_e)$. Here, the uncertainties in the total number of events cancel out. The results obtained by the four experiments are summarized in Table 1.1. While the $(\nu_\mu + \overline{\nu}_\mu)/(\nu_e + \overline{\nu}_e)$ ratio obtained

by Frèjus and NUSEX agrees with the predicted values, that measured by the two water Čerenkov experiments, IMB and Kamiokande, is significantly lower. However, as the statistical errors of the results by Frèjus and NUSEX are large, their results do not contradict with those of IMB and Kamiokande.

With a fiducial volume 5 times larger than the combined previous atmospheric neutrino detectors, Super-Kamiokande collects contained atmospheric neutrino events at a rate of about 7 per day within the fiducial volume and will soon have accumulated high statistics which allow more detailed studies. The light collection efficiency of 7 photo-electrons/MeV improves particle identification and vertex resolution. Tables 1.2 and 1.3 compare physical parameters and performance of the two previous water Čerenkov detectors with the Super-Kamiokande detector.

Table 1.2: Comparison of the physical parameters of the large water Čerenkov detectors.

PARAMETERS	KAMIOKANDE III	IMB-3	SUPER KAMIOKANDE
TOTAL MASS	4500 tons	8,000 tons	50,000 tons
FIDUCIAL MASS			
p-decay	1040 tons	3300 tons	22,000 tons
solar	680 tons	none	22,000 tons
supernova	2140 tons	6800 tons	32,000 tons
TOTAL SIZE	16 m $\times$ 19 mϕ	$22 \times 17 \times 18$ m^3	41 m $\times$ 39 mϕ
DEPTH	2700 mwe	1570 mwe	2700 mwe
# of PMTs	948 @ 50 cm	2048 @ 20 cm	11,200 @ 50 cm
		+ wavelength shifter	+2,200 @ 20 cm
PMT TIMING RESOLUTION	4 ns @ 1 pe	11 ns @ 1 pe	2.5 ns @ 1 pe
PHOTO-CATHODE COVERAGE	20%	4%	40%
	$\sim$5 pe/MeV	$\sim$1 pe/MeV	$\sim$7 pe/MeV
ANTI-COUNTER	$\sim$1.5 m	None	2.5 m
	side only		all surfaces

Table 1.3: Comparison of the performance parameters of the large water Čerenkov detectors.

PARAMETERS	KAMIOKANDE III	IMB-3	SUPER KAMIOKANDE
Threshold (trigger)	5.2 MeV	15 MeV	4 - 5 MeV
Threshold (analysis)	7.5 MeV	20 MeV	5 MeV
ENERGY RESOLUTION			
e of E(GeV)	$3.6\%/\sqrt{E}$	$3\%/\sqrt{E}$	$2.6\%/\sqrt{E}$
$\mu(\leq 1GeV)$	4%	$3\%/\sqrt{E}$	2.5%
$e(\leq 20MeV)$	$20\%/\sqrt{E/(10MeV)}$	—	$16\%/\sqrt{E/(10MeV)}$
POSITION RESOLUTION			
10 MeV e	110 cm	—	50 cm
$p \longrightarrow e^+\pi^0$	15 cm	35 cm	$\sim$ 10 cm
ANGULAR RESOLUTION			
Cosmic Ray Muons	2.7°	5°	$\sim 1°$
10 MeV e	28°	—	28°
e/μ SEPARATION	98%	92%	99%
μ DECAY DETECTION	88%	80%	95%

Chapter 2

Neutrino Physics

2.1 General Overview

The neutrino was first postulated in 1931 by Wolfgang Pauli [9, 10]. The study of beta decay had revealed that energy and momentum were not conserved by the measured decay products.

$$ {}^{A}_{Z}X \rightarrow {}^{A}_{Z+1}X' + e^{-} \tag{2.1} $$

Whereas in a two body decay like the process above energy and momentum of the outgoing particles are fixed, the energy of the electron was found to vary considerably. To resolve this problem Pauli proposed an electrically neutral particle with very small or zero mass that does not interact noticeably with matter. It was known that the spins of the the nuclei involved in beta

decay differ by 0 or ± 1 and that the electron has spin $\frac{1}{2}$, which violates angular momentum conservation. Therefore the new particle had to have spin $\frac{1}{2}$. However, Pauli's ideas were viewed with some skepticism until Fermi presented his very successful theory of beta decay.

Although the existence of the neutrino was well founded in theory, it was not proven experimentally until 1953 when Cowan and Reines announced its observation [11]. Their experiment used the intense neutrino source of a nuclear reactor. The neutrino was detected by the observation of "inverse" beta decay reactions

$$\overline{\nu} + p^+ \rightarrow n + e^+. \tag{2.2}$$

As the equation above already implies the neutrino involved is actually an antineutrino. The question whether ν and $\overline{\nu}$ are really distinct was clarified by an experiment by Davis and Harmer in the late fifties. While the reaction

$$\nu + n \rightarrow p^+ + e^- \tag{2.3}$$

had already been observed, they found that the analogous reaction

$$\overline{\nu} + n \rightarrow p^+ + e^- \tag{2.4}$$

did not occur although it should have the same cross section, if ν and $\overline{\nu}$

were identical. To distinguish neutrinos from antineutrinos Konopinski and Mahmoud introduced a *lepton* number. Electrons, muons and neutrinos were assigned the lepton number $L = +1$ whereas positrons, positive muons and antineutrinos were assigned $L = -1$. According to the law of lepton number conservation L cannot change in any interaction. In addition to their lepton number, ν and $\overline{\nu}$ also differ in their helicity: neutrinos are "left-handed" whereas antineutrinos are "right-handed".

However the concept of lepton numbers was modified in the early sixties. Brookhaven and CERN observed the process $\pi^+ \rightarrow \mu^+ + \nu_\mu$ followed by

$$\nu_\mu + n \rightarrow \mu^- + p \tag{2.5}$$

but not

$$\nu_\mu + n \rightarrow e^- + p \tag{2.6}$$

The suggested solution was to assign a muon number $L_\mu = +1$ to μ^- and ν_μ and an electron number $L_e = +1$ to e^- and ν_e, with a negative number for the corresponding antiparticles.

The Standard Model finally assumes the existence of neutrinos of three different flavors. In addition to ν_μ and ν_e, a neutrino associated with the τ-lepton is universally expected, although no direct observation of it has yet been made.

2.2 Neutrino Oscillations

In the Standard Model all neutrinos are massless. This is mainly based on experimental findings. Measurements on the exact shape of the beta-decay spectrum set limits on the electron neutrino mass $M(\nu_e) \leq 5.1$ eV [12]. Only one experiment in Moscow claimed to have measured an electron neutrino mass between 17 and 40 eV. This result is very controversial, though.

However, a zero neutrino mass is more an *ad hoc* statement and is not required by any theoretical principal. In fact most extensions of the Standard Model predict massive neutrinos. Assuming neutrinos have finite mass and their eigenstates are not identical with their weak eigenstates, neutrino oscillations occur [13].

Similar to the Cabibbo-Kobayashi-Maskawa quark mixing matrix the transformation from a neutrino flavor eigenstate to a mass eigenstate is performed via a unitary matrix U:

$$|\nu_j\rangle = \sum_{\lambda \in \{e,\mu,\tau\}} U_{j,\lambda} \; |\nu_\lambda\rangle \tag{2.7}$$

where $|\nu_j\rangle$ $j \in \{1,2,3\}$ denotes mass eigenstates and $|\nu_\lambda\rangle$ $\lambda \in \{e,\mu,\tau\}$ denotes flavor eigenstates. Mass eigenstates propagate in time according to

$$|\nu_j(t)\rangle = e^{-iE_j t/\hbar}|\nu_j(0)\rangle. \tag{2.8}$$

The transition amplitude from flavor eigenstate λ to λ' is

$$\langle \nu_{\lambda'}(0)|\nu_\lambda(t)\rangle \;= \sum_{j=1}^{3} U^{\dagger}_{\lambda',j} e^{-iE_j t/\hbar} U_{j,\lambda} \tag{2.9}$$

and the transition probability is

$$P(\lambda \to \lambda') \;=\; |\langle \nu_{\lambda'}(0)|\nu_\lambda(t)\rangle|^2. \tag{2.10}$$

In the case that one flavor state is not coupled to the other two, the equations can be decoupled into to a two-state problem and a stationary state. The transformation matrix can be parametrized as:

$$U \;= \begin{pmatrix} \cos(\theta) & -\sin(\theta) \\ \\ \sin(\theta) & \cos(\theta) \end{pmatrix} \tag{2.11}$$

if it is further assumed that CP is conserved, which allows to choose a real unitary matrix. If a ν_μ was created at time 0 the probability to observe a ν_e at time t is:

$$\begin{aligned} P(\nu_\mu \to \nu_e) &= \sin^2(2\theta)\sin^2\left(\frac{t}{\hbar}(E_1 - E_2)\right) \\ &\approx \sin^2(2\theta)\sin^2\left(\frac{(m_1^2 - m_2^2)}{2p\hbar}c^3 t\right) \end{aligned}$$

$$= \sin^2(2\theta)\sin^2\left(\frac{c^2}{2\hbar}\Delta m^2\frac{L}{E}\right) \tag{2.12}$$

where the Taylor expansion $E = \sqrt{(cp)^2 + (mc^2)^2} \approx cp + \frac{m^2c^3}{2p}$ is used, since m $\ll$ E.

The mixing phenomenon described above is known as vacuum oscillation. In the presence of matter this has to be modified as first pointed out by S. P. Mikheyev and A. Y. Smirnov using ideas developed by Wolfenstein [14]. Due to interactions with the medium, the energy eigenstates are no longer identical to mass eigenstates in vacuum. This can be described by introducing an effective mass. The ν_e acquire an extra mass term because they are the only neutrinos that can undergo charged-current elastic scattering from electrons in addition to neutral-current interactions. The effective mass is a function of the electron density of the medium. For simplicity a two flavor system is considered. If a ν_e is created in a high density environment, i.e. in the core of the sun, it primarily is in the upper energy state ν_2. If the two eigenstates ν_1 and ν_2 never come too close together the adiabatic approximation ensures that the probability for a transition from state ν_2 to ν_1 is very low as the neutrino travels to regions of lower density. In a low density environment the ν_2, however, corresponds to a ν_μ. This flavor changing process is known as MSW effect. Because of the relatively low densities in the earth and the particular parameter range of interest, this is not expected to have

a considerable effect on atmospheric neutrinos.

2.3 Atmospheric Neutrinos

For the analysis of atmospheric neutrinos it is essential to develop reliable models of their production mechanism. These have to provide quantitative predictions of flux, spectra and flavor composition of atmospheric neutrinos at the detector site.

Atmospheric neutrinos are produced by cosmic rays that produce secondary particles in the atmosphere, which decay generating neutrinos [15]. The primary cosmic ray flux is relatively well known for energies below 100 GeV. Its composition is H(proton) $\approx$ 90.6%, He $\approx$ 9.0% and CNO nuclei $\approx$ 0.3% at energies of $\approx$ 100 MeV/nucleon. For higher energies the portion of protons is even higher. The energy spectrum can be seen in Figure 2.1.

The cosmic ray flux reaching the atmosphere is influenced by solar activity and by the earth's magnetic field. The solar wind, which depends on the solar activity, drives back the low energy part of the cosmic rays. The geomagnetic field causes a shield effect, that prevents cosmic rays from arriving at the earth, if their energy is below a certain threshold, which depends on the entering position on the earth.

Cosmic rays create π's and K's via interactions with nuclei in the at-

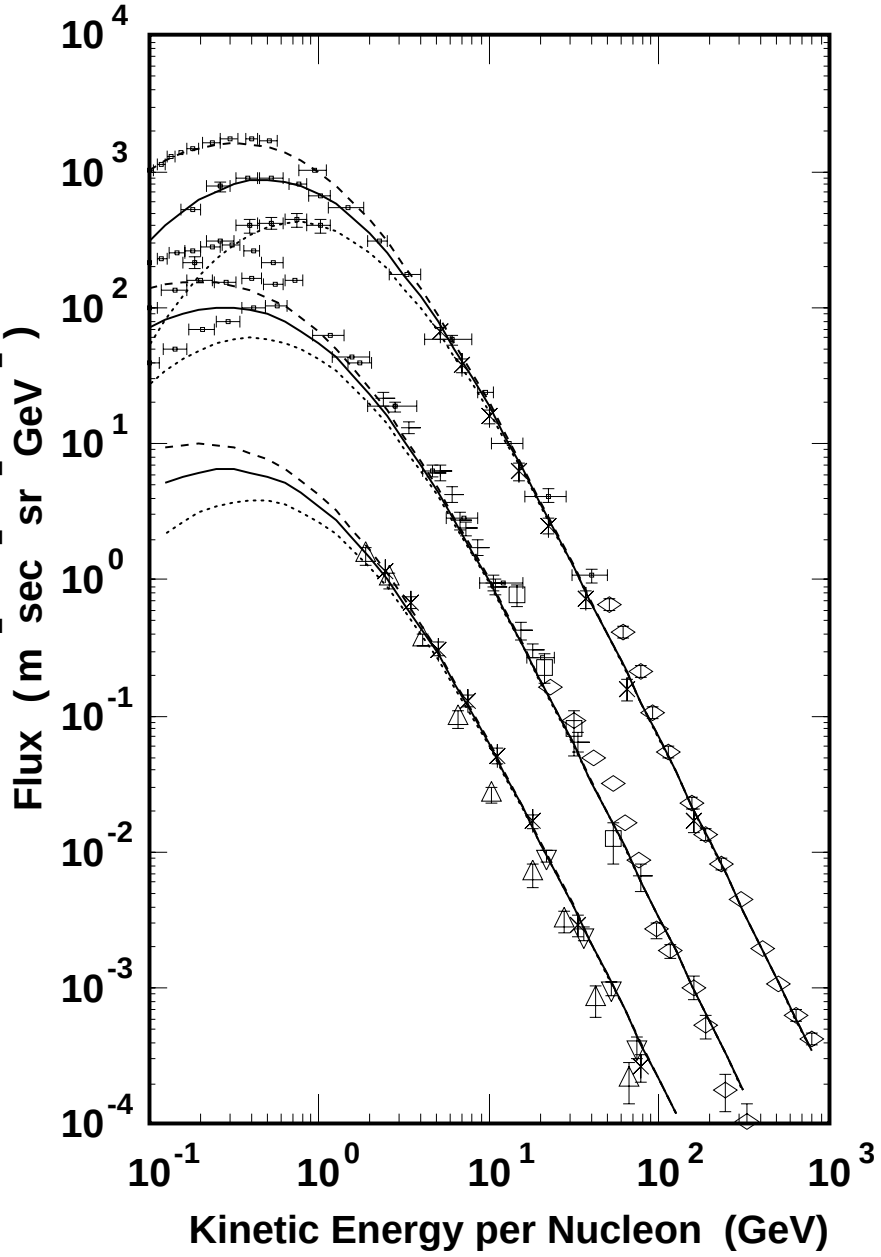

Figure 2.1: Observed fluxes of cosmic ray protons(upper curve), helium(middle curve) and CNOs(lower curve) as parametrized by Honda [15]. Solid lines are parameterization for solar mid., dash lines for solar min. and dotted lines for solar max.

mosphere. The π's account for 90% of the secondaries, thus representing the dominant source of atmospheric neutrinos. The π's decay,

$$\begin{aligned} \pi^+ &\rightarrow \mu^+ + \nu_\mu \quad (BR \approx 99.98\%) \\ \pi^- &\rightarrow \mu^- + \overline{\nu}_\mu \end{aligned} \tag{2.13}$$

and their muon secondaries also decay,

$$\begin{aligned} \mu^+ &\rightarrow e^+ + \nu_e + \overline{\nu}_\mu \\ \mu^- &\rightarrow e^- + \overline{\nu}_e + \nu_\mu . \end{aligned} \tag{2.14}$$

Naively one would expect the following ratios by just counting the decay neutrinos,

$$\frac{\nu_\mu + \overline{\nu}_\mu}{\nu_e + \overline{\nu}_e} \approx \frac{2}{1} \tag{2.15}$$

and

$$\frac{\nu}{\overline{\nu}} \approx \frac{1}{1} \tag{2.16}$$

However, these ratios depend on the energy of the neutrinos. For high energies $(\nu_\mu + \overline{\nu}_\mu)/(\nu_e + \overline{\nu}_e)$ is larger than 2, because the muons are highly relativistic and many of them do not decay on their way to the detector

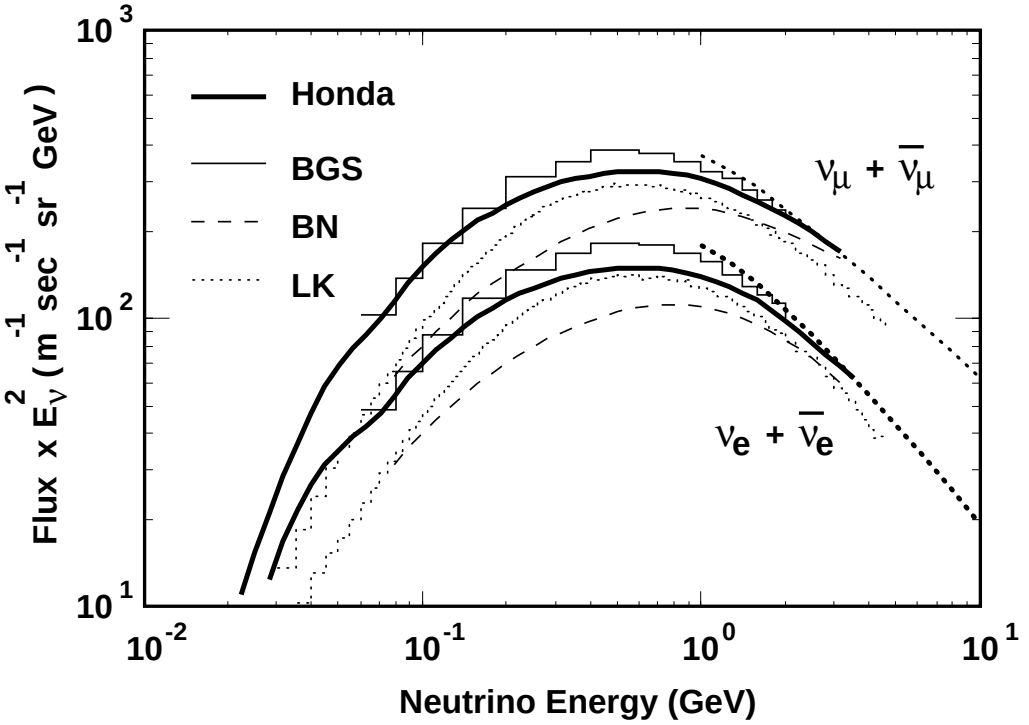

Figure 2.2: Atmospheric ν-fluxes multiplied by E_ν^2 for the Kamiokande site at solar mid.. Calculations by four different authors are shown: Honda [15]; Barr, Gaisser and Stanev (BGS)[16]; Bugaev and Naumov (BN)[17]; Lee and Koh (LK)[18]. (from [15])

(mainly due to interactions), which means that no ν_e was created. A thorough study includes interactions of π's and μ's with matter, a correct 3-dimensional geometry and the fact that μ's created in π-decays are fully polarized.

The flux of atmospheric neutrinos at different positions on the surface of the earth has been calculated by many authors [15, 16, 17, 18] using different techniques. Figure 2.2 shows the results of four calculations for the Kamioka site. The results in the total flux in the energy range 100 MeV

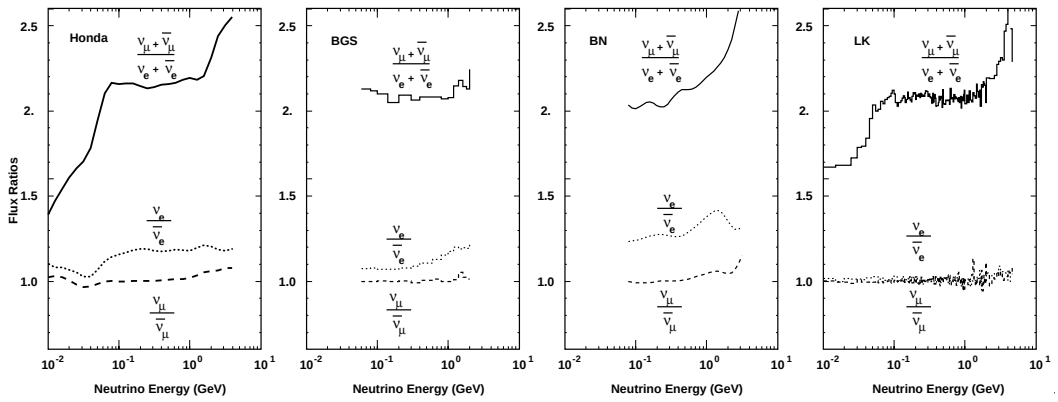

Figure 2.3: The flux ratio of ν-species calculated for Kamioka by the same authors as in Fig. 2.2. (from [15])

to 10 GeV vary by over 30% due to the use of different primary fluxes and different interaction models. However, most uncertainties cancel out for the ratio $(\nu_\mu + \overline{\nu}_\mu)/(\nu_e + \overline{\nu}_e)$ and the predictions disagree by only a few percent in the energy range of interest. Figure 2.3 shows the energy dependence of $(\nu_\mu + \overline{\nu}_\mu)/(\nu_e + \overline{\nu}_e)$ as predicted by several studies.

2.4 Interaction with Matter

Atmospheric neutrinos are detected through their interaction with matter. To compare the predicted atmospheric neutrino flux with the measured event rates, the physics of neutrino interactions has to be studied in detail.

In general three different classes of interactions of neutrinos with water can be distinguished: elastic scattering off electrons, quasi-elastic scattering off nucleons and inelastic interactions with nucleons. They can further be

classified as charged-current (CC) or neutral-current (NC) weak interactions. The tree level Feynman-diagrams for these processes are shown in Fig. 2.4, 2.5 and 2.6. Cross sections for elastic scattering off electrons can be calculated using the standard electroweak theory. The total cross section off electrons is higher for ν_e's than for ν_μ's or ν_τ's because they have additional W-exchange channels available. The inverse muon decay is only possible for very high ν_μ-energies ($E \geq 11$ GeV). However the neutrino-electron cross section is much lower than the neutrino-nucleon cross section (roughly by the mass ratio m_e/m_p).

In the energy range $E_\nu \leq 1$ GeV the quasi-elastic neutrino-nucleon interactions are the dominant mode. Neutral current elastic interactions, however, are practically invisible for water Čerenkov detectors, as the recoil nucleon rarely has enough energy ($E_\nu \geq 1.5$ GeV) to generate Čerenkov light. Charged-current quasi-elastic interactions can be described using the standard V - A theory. The lepton momentum and energy in the final state can be determined by the q^2 ($q = p_\nu - p_{lepton}$; 4-momentum transfer) dependence of the cross section. Figure 2.7 shows the energy dependence of the charged-current quasi-elastic cross section.

At higher energies ($E_\nu > 340$ MeV), resonance states heavier than the neutron or proton can be created, which decay into a nucleon and one or more pions. This interaction is called inelastic scattering. For single pion

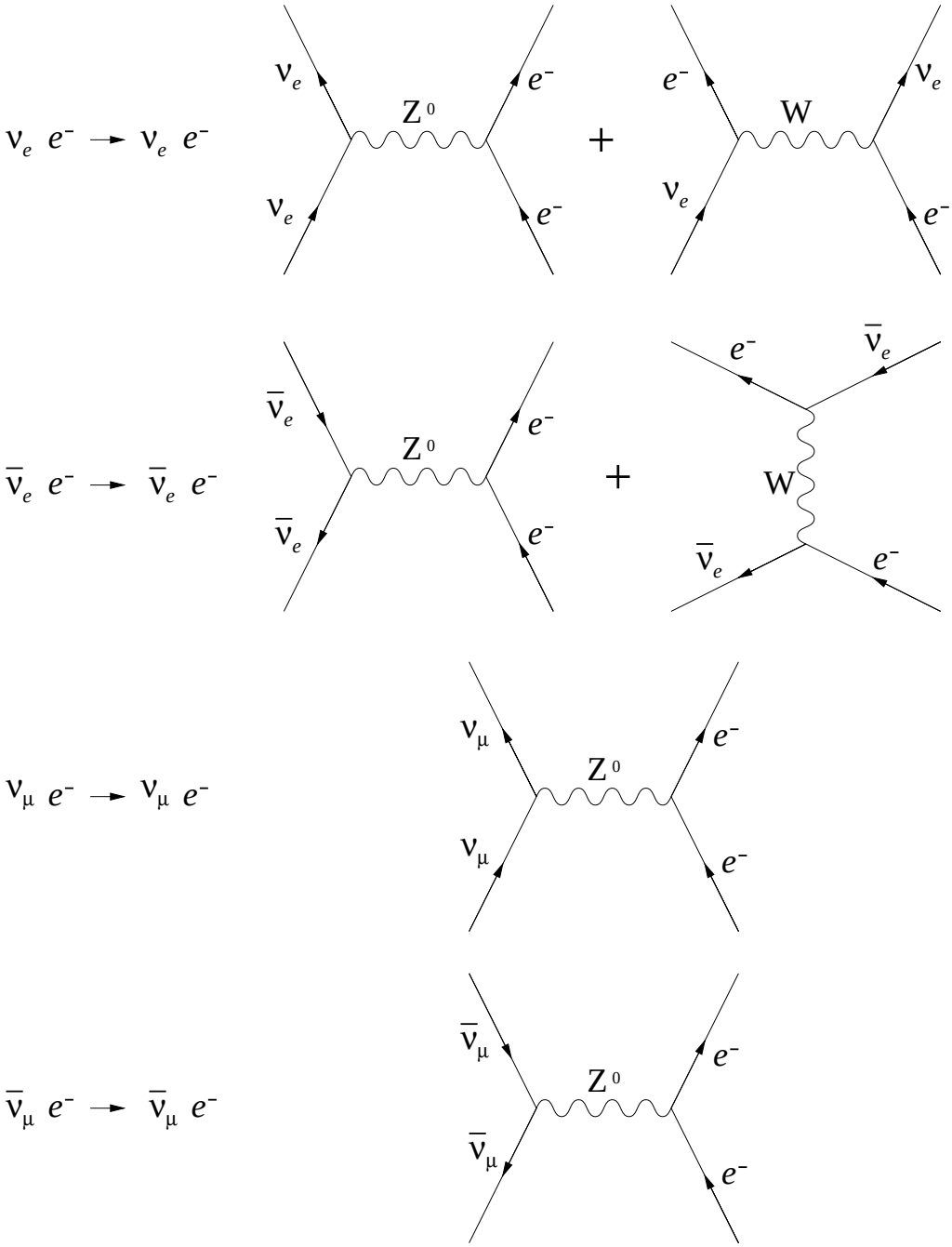

Figure 2.4: Tree level Feynman diagrams for elastic νe scattering

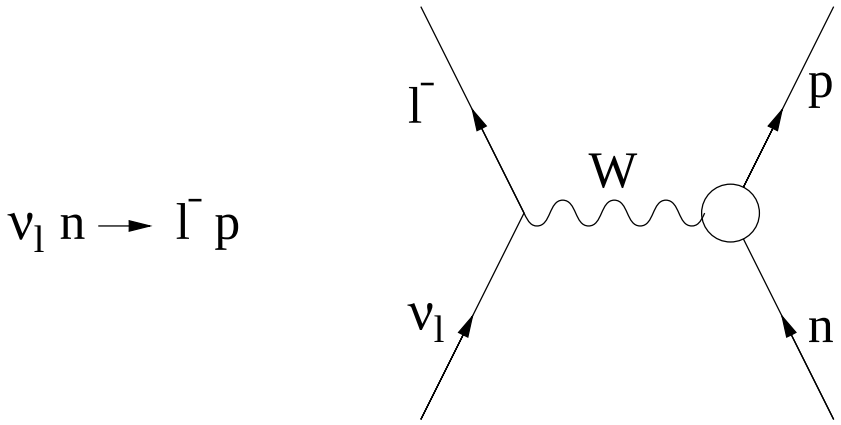

Figure 2.5: Tree level Feynman diagrams for quasi-elastic νN scattering

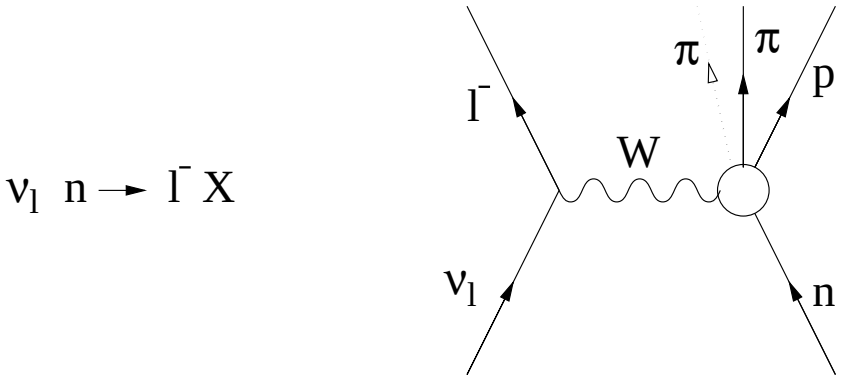

Figure 2.6: Tree level Feynman diagrams for inelastic νN scattering

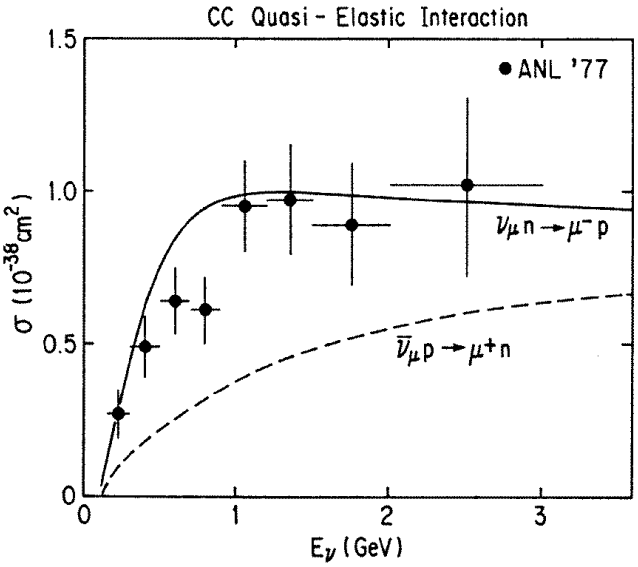

Figure 2.7: Cross section of charged-current quasi-elastic interactions off free nucleons (from [3]).

production satisfactory models have been developed [20, 21]. Cross sections according to the model of Fogli and Nardulli are shown in Figure 2.8.

For neutrino energies above 1 GeV multiple pion producing inelastic interactions are frequent. Their theoretical description is not easy because of the large number of possible final states. However, it is expected that the cross-section rises linearly with energy. The mean multiplicity of charged hadrons as determined by high-energy experiments can be parameterized as a function of the hadronic invariant mass W by $\langle n_\pi \rangle = 0.09 + 1.83\ln(W^2)$. The total cross-section of charged-current interactions can be seen in Figure 2.9. The ratio of $\sigma(\nu_\mu : CC)/\sigma(\nu_e : CC)$ is shown in Figure 2.10. As expected

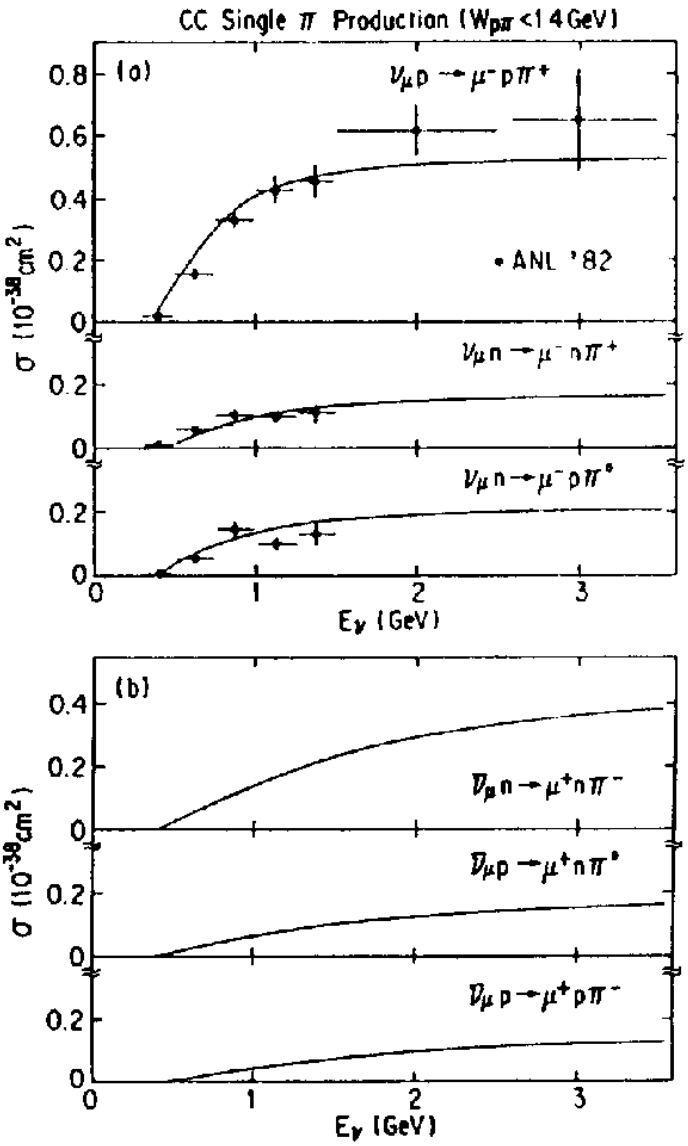

Figure 2.8: Cross section for charged-current single-pion production (from [3]).

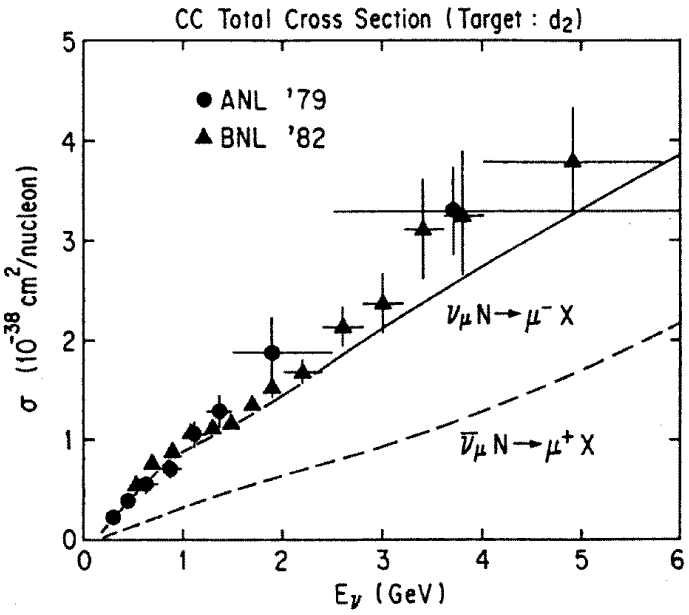

Figure 2.9: Total cross section for charged-current interactions (from [3]).

the ratio approaches unity for large energies.

Effect of the Nucleus

So far it has been assumed that the neutrinos interact with free nucleons. The cross sections for low energy neutrino interactions with water have to be modified because 89% of the nucleons are bound in oxygen nuclei. Bound nucleons are affected by their Fermi momentum and the energy levels of the nucleus. This influences the energy that the nucleon provides to the interaction. The simplest model to account for bound nucleons is the "Fermi gas model". It assumes a characteristic momentum distribution for each

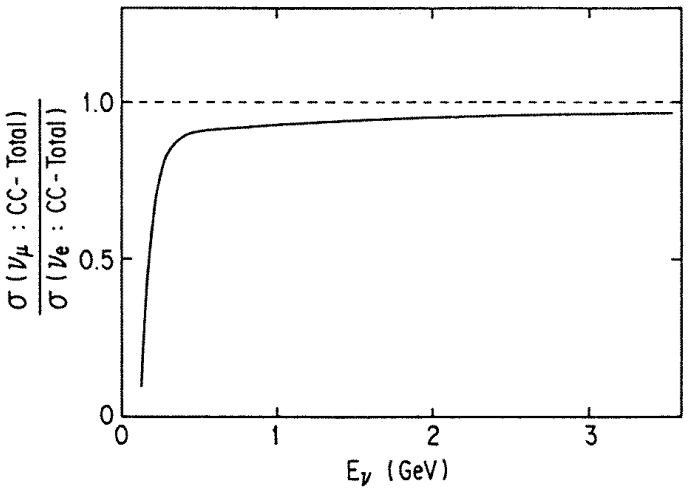

Figure 2.10: Ratio of the CC total cross section between ν_e and ν_μ (from [3]).

bound nucleon. In oxygen the average momentum is about 175 MeV.

For low energy interactions Fermi statistics have to be taken into account. As the energy states below the "Fermi sea" are already occupied, they are not available for outgoing nucleons, by the Pauli exclusion principle. This so called "Pauli blocking" reduces the overall cross section. Figure 2.11 compares the cross sections off a free nucleon and a bound nucleon.

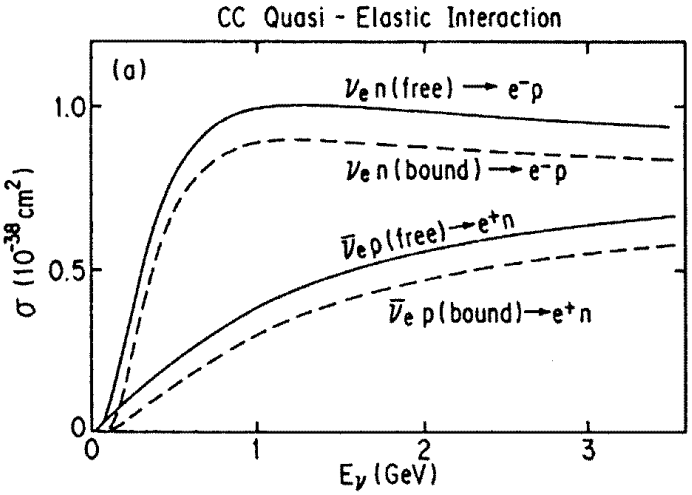

Figure 2.11: Comparison of the calculated cross section of CC quasi-elastic interactions off a free nucleon and a bound nucleon in ^{16}O (from [3]).

Chapter 3

Detector Description

3.1 Basic Principle of a Water Čerenkov Detector

Super-Kamiokande is a ring imaging water Čerenkov Detector. The basic detection principle is based on the fact that charged particles with sufficient velocity radiate Čerenkov light when passing through a dielectric medium [22, 12]. The threshold velocity depends on the index of refraction of the medium and is given by:

$$\frac{v}{c} = \beta \geq \frac{1}{n} \tag{3.1}$$

The Čerenkov light is emitted at a certain angle called the Čerenkov angle Θ_c given by:

$$cos\Theta_c = \frac{1}{n\beta} \tag{3.2}$$

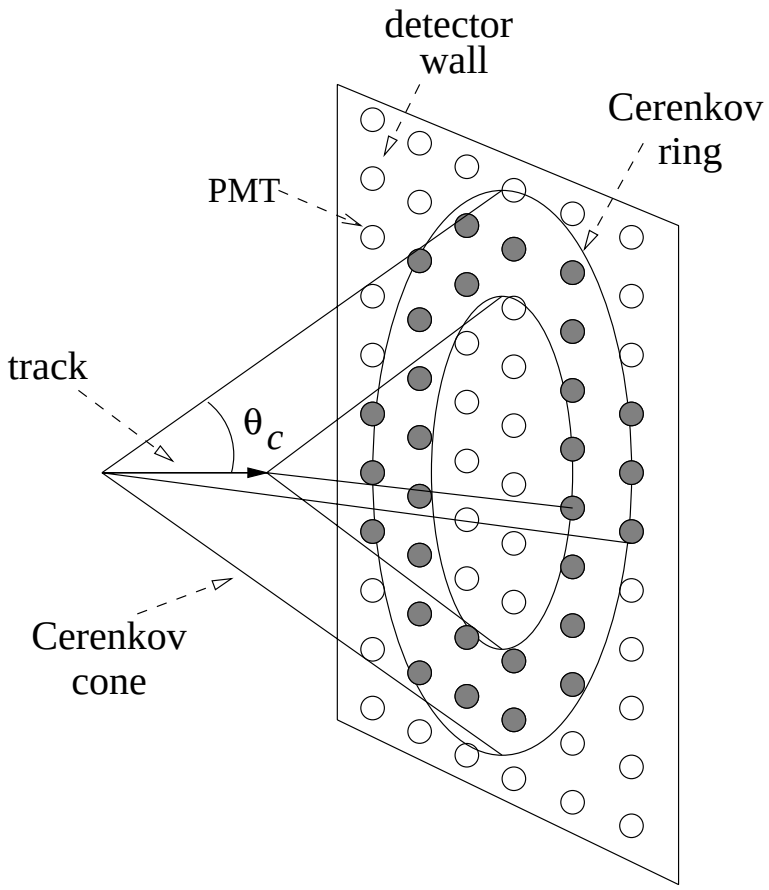

Figure 3.1: Čerenkov geometry

The geometry of the Čerenkov cone can be seen in Figure 3.1. In water the Čerenkov angle has a maximum value of 42^0 for highly relativistic particles ($\beta = 1$) in the visible light region.

The spectrum of emitted light has a continuous $1/\lambda^2$ dependence. The number of photons emitted per unit length for a particle of charge z is:

$$\frac{d^2N}{dxd\lambda} = \frac{2\pi\alpha z^2}{\lambda^2}\left(1 - \frac{1}{\beta^2 n^2(\lambda)}\right) \tag{3.3}$$

or,

$$\frac{d^2N}{dEdx} = \frac{\alpha z^2}{\hbar c} sin^2\Theta_c \quad (3.4)$$

$$\approx 370\ sin^2\Theta_c\ eV^{-1}cm^{-1} \quad (z=1) \quad (3.5)$$

The spectrum however is not infinite since the index of refraction in water approaches unity for higher frequencies, which leads to a cut-off in the spectrum. In the sensitive wavelength range of the photomultipliers (300 nm $\leq \lambda \leq$ 600 nm) a $\beta = 1$ single-charged particle emits 766 $sin^2\Theta_c$ ($\approx$ 343 in water) photons per cm.

3.2 The Water Tank

The Super-Kamiokande detector is situated in the Kamioka mine (the same mine as Kamiokande) 250 km west of Tokyo. It is shielded by a minimum of 1000 meters rock with an average density of $2.7g/cm^3$. This determines a minimum energy of about 1.3 TeV, which muons must have at the surface to reach the detector. It also reduces the cosmic ray muon flux at the detector by a factor of 10^5.

The water tank is constructed inside a cylindrical excavation of 39 meters in diameter and 58 meters in height (including 15 meters of dome) (see Figure 3.2. Its side walls, top and bottom are lined with 40 to 50 cm of

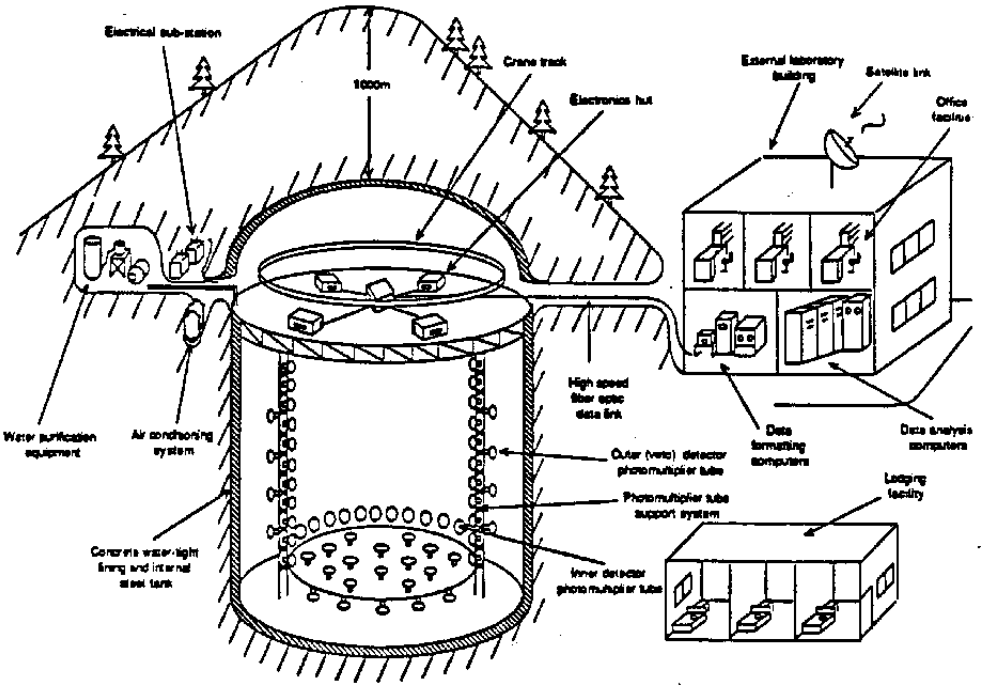

Figure 3.2: Schematic diagram of Super-Kamiokande

reinforced concrete. On this uniform structure a layer, consisting of 3 to 4.5 mm of welded stainless steel, is mounted. This provides a water- and airtight barrier. At a height of 41 meters a flat roof forms the top of the actual water-filled detector vessel. The tank is filled with a total of 50,000 tons of pure water. The region above the tank is accessible and contains the high-voltage supply system, the data acquisition and control computers and other equipment.

The photomultiplier support system consists of a stainless steel structure, 2.5 meters from the walls, bottom and top of the cavity. It optically

divides the tank into an inner part, 36.20 meters high and 33.80 meters in diameter (32 ktons), and an outer shell of 2 meters thickness. 11,146 50-cm inner phototubes are mounted on the support system facing inwards. They provide a total light coverage of 40% of the inner detector surface. 1,857 20-cm outer tubes, facing outwards from the support structure, are used as an anti-counter to veto events that enter the detector from outside. A layer of black polyethylene sheets, which is set behind the inner phototubes, optically isolates the inner detector. All surfaces of the outer detector are covered with a white tyvek layer of high reflectivity to increases the light collection efficiency.

A "radon-free" atmosphere is maintained by an air-filtration system and a supply of fresh, low radon air from outside the mine. The background radioactivity of the water is also reduced by the water purification system. In about one month the water in the entire detector is recirculated through a filtering system. Heavy radioactive particles and small particles are removed. In addition to that, water from outside the mine is filtered by reverse osmosis. To prevent bacterial growth the water is sterilized with ultra-violet light. A water temperature of 11^0 C helps to suppress biological contamination. With these combined techniques a water attenuation length of 60 meters has been achieved.

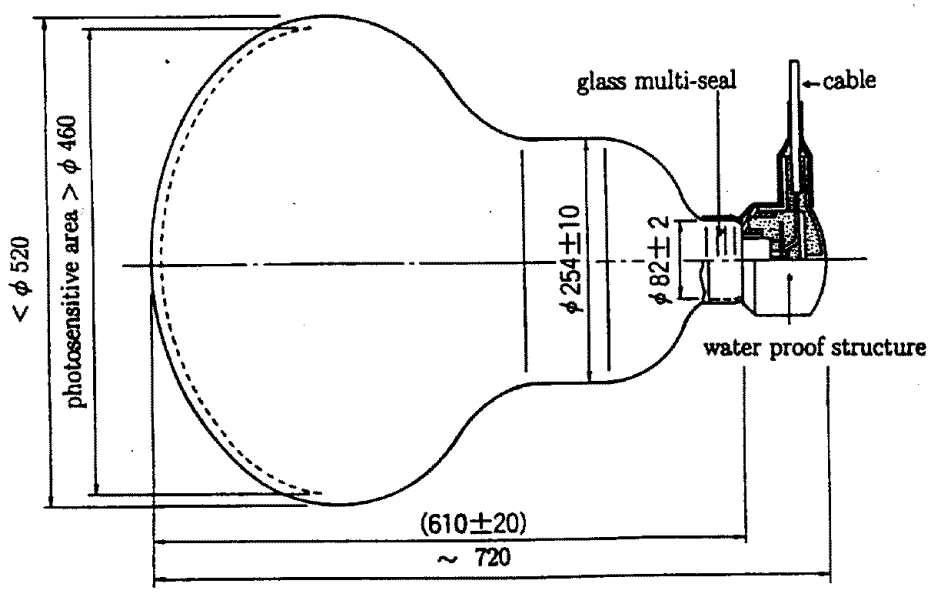

Figure 3.3: The 50 cm Photomultiplier Tube

3.3 Photomultipliers

Two different photomutiplier (PMT) types are used for the inner and outer detector. The inner detector is equipped with 11,146 Hamamatsu R1449 tubes, 50-cm in diameter. 1,857 20-cm Hamamatsu R1408 PMTs are installed in the outer detector.

Inner Tubes

The inner PMTs are an improved version of the ones used in the Kamiokande detector [23]. The new tubes (Figure 3.3) are equipped with a quasi-hemispherical window with a bi-alkali (Sb-K-Cs) coating on the inside of the bulb, called

Figure 12: Quantum efficiency.

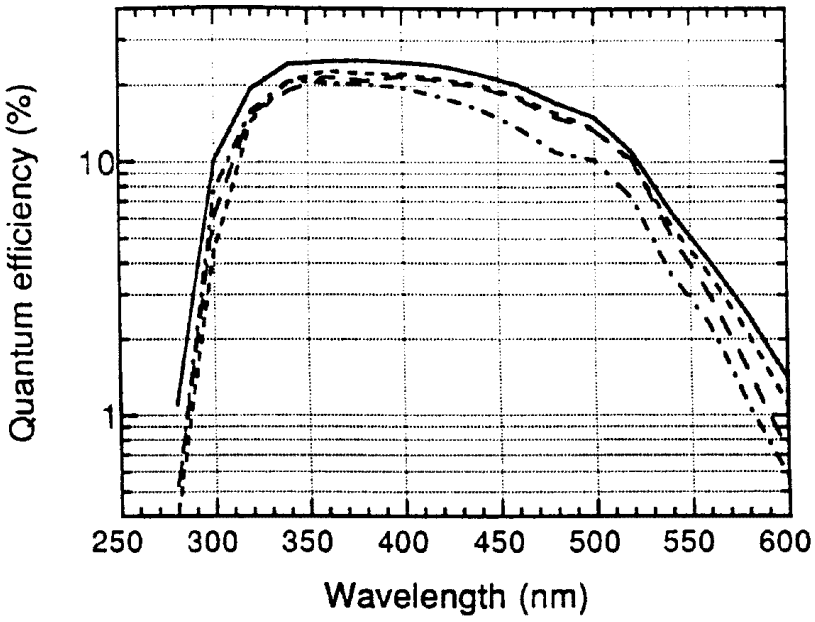

Figure 3.4: Quantum Efficiency of a 50 cm PMT

the photocathode. When a photon hits this layer an electron can be emitted by the photo-electric effect. The probability to knock off an electron (the quantum efficiency) is a function of the wavelength of the light, depending on the photocathode material and the permeability of the window. As can be seen from Figure 3.4, the maximum quantum efficiency is 22% at $\lambda = 390$nm. Primary photoelectrons from the cathode are accelerated by an electric field to a series of plates called "dynodes", which are ordered like layers of venetian blinds in the back of the PMT. When the photoelectron (pe) hits the first dynode-layer, it has enough energy to create ~ 5 secondary electron.

These are again accelerated to the second dynode, where they create more electrons. After 11 dynode stages the average gain, which is defined as the ratio of the anode-current to the cathode-current, is 10^7 at a total applied voltage of 2000 volts. The collection efficiency, which is the probability that a primary pe creates a large enough pulse at the anode, has been determined to be about 70%.

The improvement of the new PMTs focused on the reduction of the time jitter and the improvement of the energy resolution, the two most important characteristics for event reconstruction in an imaging Čerenkov detector. For a voltage of 2000 V the transit time (time from the emission of the photo-electron to the appearance of the anode-pulse) is about 100 nsec. A time jitter (at 1 pe light level) of $\leq$ 3 nsec (1 σ) has been measured, which is considerably smaller than the value for the older model. The anode-pulse response to a δ-function shaped input light has rise- and fall-times of about 10 nsec and a full width half max. of 18 nsec. Energy resolution has also been improved greatly. The pulse height distribution shows a single-pe peak well separated from the dark noise peak. This allows the experiment to reduce the energy threshold to 5 MeV.

PMT performance is sensitive to external magnetic fields, so the earth's magnetic field is compensated by 26 coils, attached to the outer walls of the detector. The field is kept at a value below 100 mG, as required for the

phototubes.

After 4 months of run time, the average dark noise rate for an individual PMT, which is mainly due to thermionic emissions of electrons from the photocathode or the dynodes, has gone down to 3 kHz. Afterpulses, broad pulses tens of μsec after the tube-hit, are found to have amplitudes $\sim 0.4\%$ of the primary pulse.

Outer Tubes

For the outer detector the tubes from the IMB experiment are reused. To increase the photo-sensitive area, each outer PMT is equipped with a 60 cm $\times$ 60 cm wavelength shifter plate. Photons in the wavelength range of 300 nm to 400 nm are absorbed by the wavelength shifter material and isotropically re-emitted with a longer wavelength. Some fraction of these secondary photons is internally reflection to the PMT, where they can be detected.

3.4 Trigger System and Data Acquisition

The electronics in the back of the inner phototube divide the voltage between the 11 dynodes and the anode as shown in Figure 3.5. The AC PMT-signal is decoupled from the DC high voltage by a capacitor and then

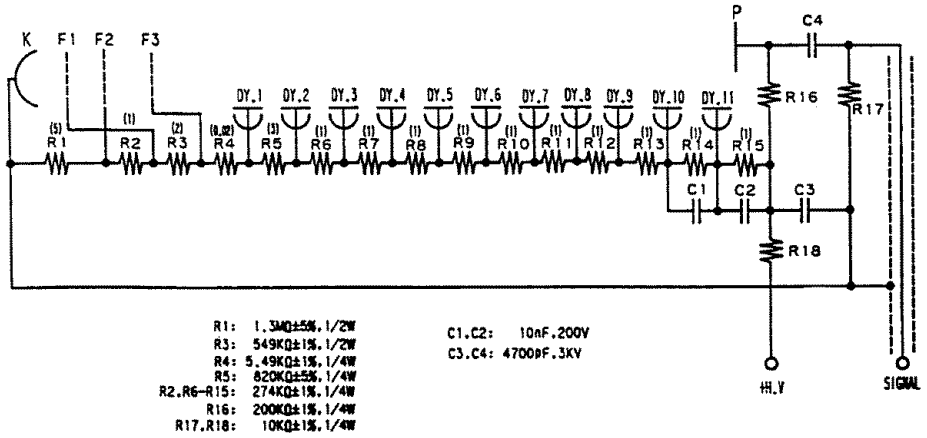

Figure 3.5: Inner PMT circuit and signal decoupling

send to the readout electronics though a coaxial cable.

Front-end Electronic System

ATMs (Analog Timing Modules) are used as "front-end" electronics for the inner phototubes. Each ATM handles 12 PMT channels. Its main purpose is to record charge and arrival time of the incoming PMT pulses. Each channel has an amplifier and a discriminator. When a PMT signal exceeds the threshold value ($\sim$ 1/5 pe), the discriminator sends a 400 nsec wide gate signal to the charge integrator, which integrates a 200 nsec delayed copy of the PMT pulse. The time is measured by integrating a constant current, which starts with the above signal and lasts until a global trigger arrives. Another output of the discriminator is a 200 nsec wide rectangular signal, which is summed for all 12 channels giving a HITSUM signal. This is used for the

global trigger. A diagram of the analog input circuit is shown in Figure 3.6. If a global trigger signal arrives before 1200 nsec after the discriminator signal, time and charge information, which are stored in capacitors, are converted to 12-bit digital data and written into a 1Kword FIFO memory together with an event number. It takes about 5 μsec to complete the digitizing. To avoid deadtimes due to the readout time, two identical sets of input circuits are used. Channel B handles any signal if Channel A did not complete digitizing the previous one. Thus two rapidly successive events, e.g. muon and decay electron ($\tau = 2.2\mu$sec), can be recorded.

Online Data Acquisition

The data acquisition system collects the time and charge data from the ATM modules. A schematic diagram can be seen in Figure 3.7. Each of the four electronic huts contains two Sun SPARClassic (S4/CL) and 240 ATM modules. A Super Memory Partner (SMP) module with 2 Mbytes internal memory collects the data output of 20 ATM modules. One S4/CL reads out the data of 6 SMP modules. The data is then transfered to the central hut. There, a Sun SPARCstation 10 (S4/10) "builds" the event by concatenating all signals belonging to one global trigger. Finally the data is sent to the offline site.

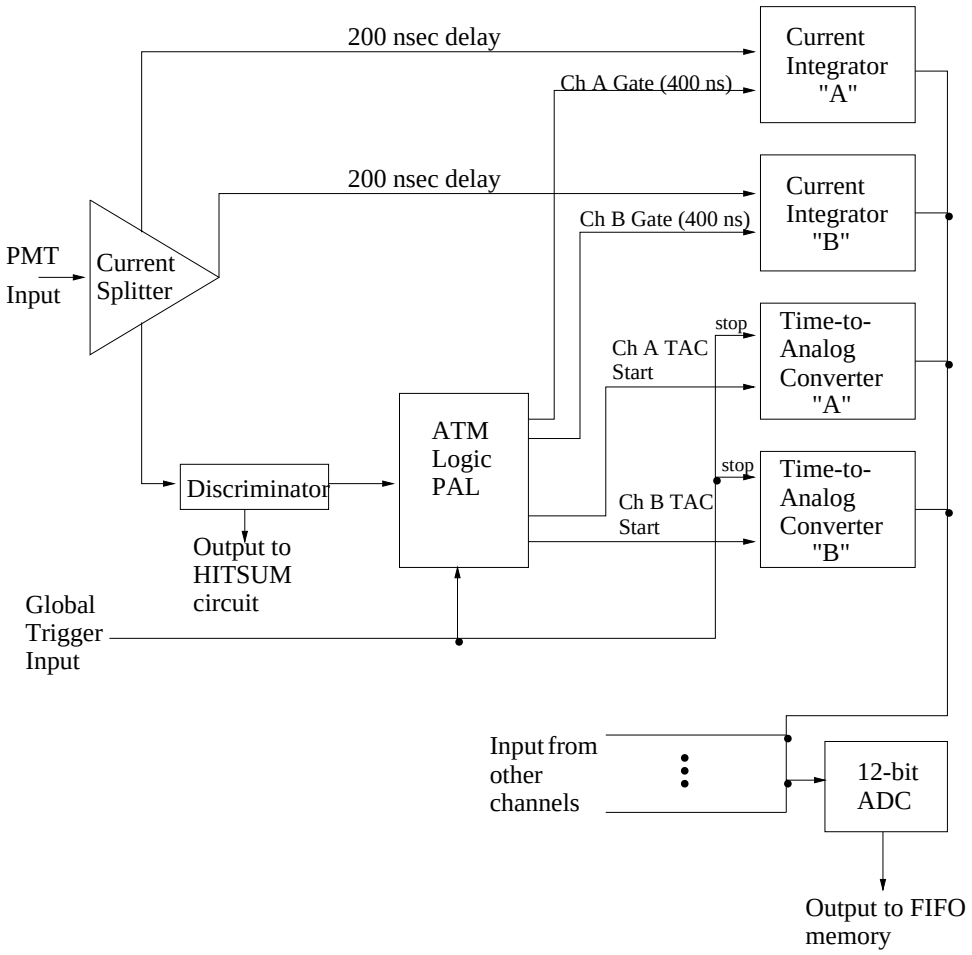

Figure 3.6: The analog input circuit of the ATM.

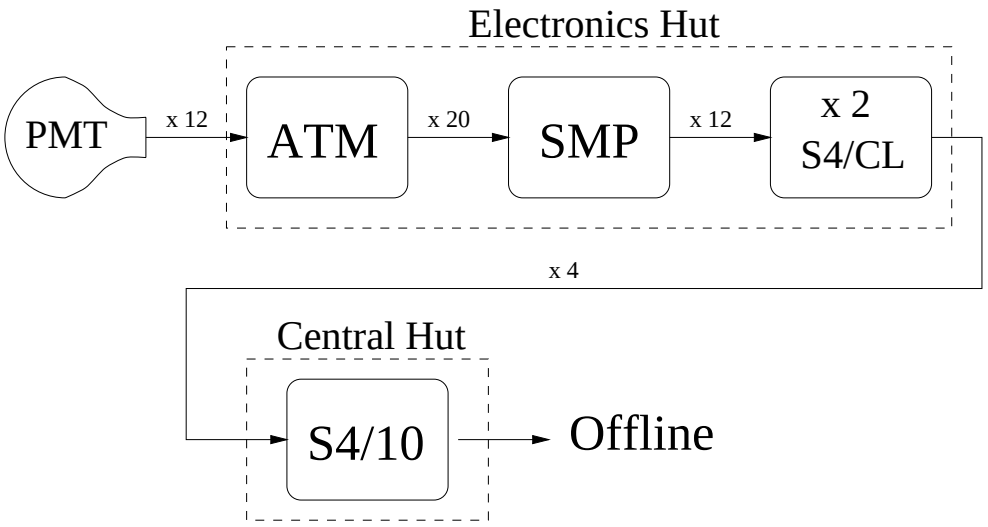

Figure 3.7: Schematic diagram of the Data Acquisition system.

Trigger

For the inner detector trigger, the HITSUM outputs of all 240 ATMs in each electronic hut are put in an analog sum. This signal is then sent to the TRG module in the central hut. The quasi-analog sum of the signals from the 4 electronic huts is compared to a trigger threshold value. Trigger signals and event counters are then distributed to 48 GONG (GO/NoGo) modules, which distribute those signals to the ATM modules. Currently the trigger threshold is set to an equivalent of 29 tube-hits, which corresponds to about 5 $\sim$ 6 MeV of visible energy. This means that a global trigger is produced if 29 tubes are hit within a 200 nsec time span. Having a background radioactivity from Radon decay ($^{222}Rn \rightarrow\ ^{214}Bi \rightarrow \beta(E_{max} = 3.26MeV)$) of 0.03 $\sim$ 0.04 Bq/m^3, the trigger rate is 10 $\sim$ 12 Hz.

Outer Detector

Signals from outer 20-cm PMTs are decoupled in a special HV decoupling card, which is connected to a QTC (Charge to Time Converter) in the electronic huts. One QTC handles the input of 48 PMTs. For each PMT there is a logical output, with a short pulse, marking the time, followed by a longer variable width pulse, encoding the charge. The width of the second pulse is (after subtracting a pedestal) proportional to the PMT charge, integrated over the 200 nsec gate period. The PMT threshold corresponds to 1/4 photo electrons. In addition, the module provides an analog HITSUM output, whose amplitude is proportional to the number of PMTs over threshold during a coincidence window of 200 nsec. Also, a logical output is provided when the HITSUM for this module is above a separate adjustable threshold.

80 QTC output channels are fed into a TDC (Time to Digital Converter), where the time and charge information is digitized. If there is a global trigger, this data is buffered on an on-board computer. Finally this is read out by the computer in the central hut.

The analog HITSUMs from the QTCs are used for an outer detector trigger, to detect events, that do not enter the inner detector. The Trigger threshold is set to an equivalent of 16 coincident PMTs (in a 200 nsec window).

Chapter 4

Analysis

4.1 Monte Carlo

Monte Carlo is the standard technique for physics simulations using random numbers. Like most physics experiments nowadays, Super-Kamiokande developed simulation programs of the detector's response to high-energy particles. These are useful for several reasons.

- Some calibration techniques are based on comparisons between real and simulated data.
- Development and testing of analysis software usually requires the use of simulated events.
- In order to compare experimental results to theoretical predictions, the efficiency of the detector for different types of events is determined

using Monte Carlo methods.

The Monte Carlo programs currently used by the US collaboration simulate events in reasonably good agreement with data, although some details and parameters still need to be adjusted. A complete simulation involves several stages:

- Generation of the initial particles and their physical state (e.g. electron and recoil proton from a ν interaction).
- Propagation of particles in the nucleus (if appropriate).
- Propagation through the detector volume including interactions with water and other detector material.
- Generation and propagation of Čerenkov light from charged particles.
- Detection of Čerenkov photons and electronics response.

For many purposes the initial-state particles are selected according to simple positional, directional or energetic constraints using a program called "kinem". For instance, this can generate a set of monoenergetic electrons uniformly distributed through the detector. For proton decay and neutrino events the first two items require more sophisticated simulations. For this purpose a program developed by the IMB collaboration is used, in this work called "Kinematics" [7].

The data of initial states is then processed by the detector simulating program "gtrack". The output are files with simulated data in the same format as real data.

Generation of Initial-state Particles with Kinematics

Flux and spectrum of neutrinos at the detector site are important inputs to the simulation of neutrino induced events. "Kinematics" uses calculations for the IMB detector location by Lee and Koh [18]. Due to the effect of the geomagnetic field the total flux for the Kamioka mine is considerably different. Therefore, "Kinematics" can not be used for any efficiency calculations or to compare measured and predicted event rates. However, the shape of the spectrum as well as the ν_μ to ν_e ratio are similar for both sites as can be seen from Figure 4.1. For neutrino interactions only the dominant scattering with nucleons is used. Elastic, quasi-elastic as well as single and multiple pion production are simulated using cross sections described in section 2.4. Hadrons created inside oxygen nuclei are tracked through the nucleus in steps of 0.1 fm. They may be scattered or absorbed producing secondary outgoing particles. A Fermi gas model is used and Pauli-blocked states are eliminated.

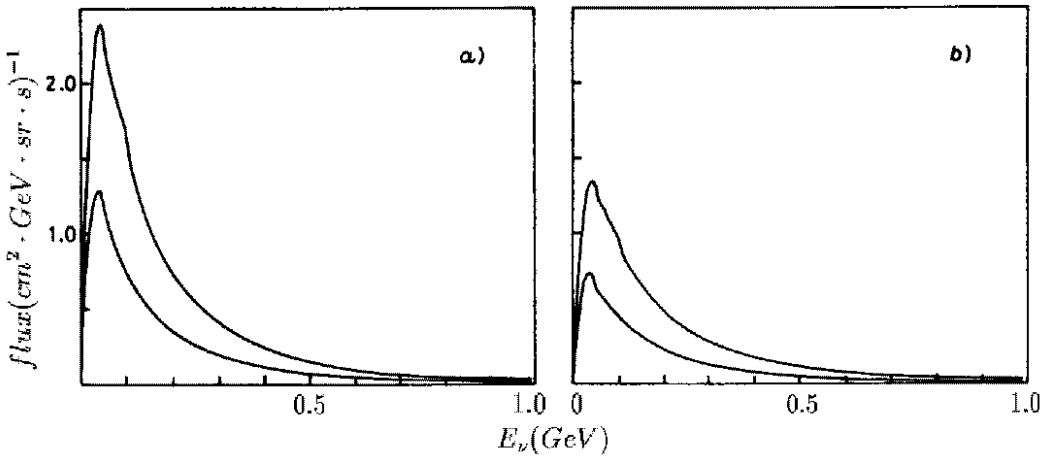

Figure 4.1: Neutrino flux averaged over 4π solid angle at *a*) Cleveland and *b*) Kamioka for solar mid.; upper curve: ν_μ, lower curve: ν_e

Tracking and Light Simulation

The core of the simulation step that tracks particles through the detector is "GEANT". This program has been developed at CERN and continuously been improved since 1974. For hadronic interactions, several software packages are available, where GHEISHA is the one used for the Monte Carlo events in this work.

A light-tracking program has been developed, based on programs written by the IMB collaboration. For each tracking step in GEANT, Čerenkov photons are created according to the angular and energetic distribution discussed in Section 3.1. Photons are then tracked through the tank including absorption and scattering in the water, reflection and absorption from walls and phototubes, as well as PMT response. Interactions are performed one

photon at a time until it is absorbed or observed. A path length is calculated for every relevant process of the photon propagation. The physical process that corresponds to the shortest of these lengths is then simulated.

Once a photon is absorbed by a PMT it may emit a photoelectron. The simulation of the subsequent electronics response is mainly bookkeeping. An event is created if the number of hits in a 200 nsec time window exceeds the trigger threshold.

Many parameters involved in the above processes have already been measured to some precision. Nevertheless, the Monte Carlo has not yet been tuned by comparison with data.

4.2 Fitting

An essential part of the analysis of the Čerenkov ring pattern produced by fast charged particles in the detector is the reconstruction of the event. Using the timing and geometrical information provided by the PMTs, the original track of the particle has to be determined. Different programs have been developed, mostly concentrating on fitting specific types of events. From the point of view of physics and analysis the following event classification will be used:

contained events: The Čerenkov light emitting particle is created inside the fiducial volume (e.g. by a ν interaction) and slows down below Čerenkov threshold before leaving the inner detector.

partially contained events: The particle is created in the fiducial volume, like in a contained event, but exits the inner detector.

through going events: A highly energetic particle (almost exclusively a cosmic ray muon) enters and exits the detector.

stopping events: A particle enters the detector and stops inside the inner detector.

The fiducial volume, in this work, is defined as the space 2 meters inside the inner detector walls. An additional classification of events is based on the number of visible Čerenkov rings in an event. For the purpose of this work mainly single-ring and multiple-ring contained events are distinguished.

Fitters for through going and stopping events are important tools for event selection and analysis of low energy events (mainly solar neutrinos).The programs described below, however, are mainly developed to reconstruct contained events.

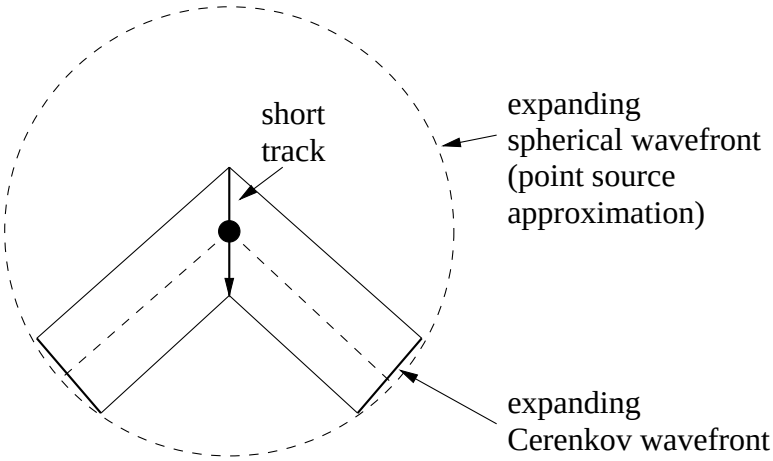

Figure 4.2: Point source timing approximation of a short, Čerenkov light emitting track

Point Fitters

Point fitters are usually the first step in any fitting procedure because they are fast and give a reliable approximation of the event vertex. They rely on the fact that the timing of a short Čerenkov radiating track is similar to the timing of a point source. The position of the best fit is, however, rather in the middle of the track, which is usually not the vertex of the event. This can be seen in Figure 4.2.

Given a trial point-source at position $\vec{X}_p$ and time T_p, the residual r_i for a PMT at position $\vec{x}_i$ that was hit at time t_i is given by:

$$r_i = T_p - t_i + \frac{|\vec{X}_p - \vec{x}_i|}{c_{water}} \tag{4.1}$$

This is the difference between the time the PMT is hit, assuming a point

source, and the actually measured time value. The vertex finding program minimizes the χ^2 of the residuals:

$$\chi^2 = \sum_{tubes\ \ i} \left(\frac{r_i}{\sigma_i}\right)^2 \tag{4.2}$$

σ is mainly determined by the time jitter of the phototube, which decreases with the amount of collected charge.

The program "Anistrack" minimizes a quantity similar to χ^2 with slightly different normalization [1]. The minimum is found by repeatedly stepping a certain distance in direction of the gradient, until an optimal value is found. Using only tubes in the residual peak of the previous vertex fit, this whole minimizing procedure is repeated with smaller step-sizes until a step-size of 10 cm is reached.

Once a vertex position is found, a good approximation for the direction of a single track is given by the anisotropy[2] vector of the event:

$$\vec{A} = \frac{\sum_i \frac{(\vec{x}_i - \vec{X}_p)}{|\vec{x}_i - \vec{X}_p|} q_i}{\sum_i q_i} \tag{4.3}$$

where $\vec{x}_i$ and $\vec{X}_p$ are defined as above and q_i is the charge of tube i. The

[1] The actual minimizing function is called pands.

[2] Anisotropy can also be used to determine the net momentum of an event. In particular it is a measure of how isotopic the event is.

direction of $\vec{A}$ is the mean direction of the emitted Čerenkov light. Because of the geometry of Čerenkov light this corresponds to the direction of the particle momentum, in the case of a single track event.

Track Fitters

Track fitters are designed to determine the position of the vertex and the direction of the track as accurately as possible, taking into account the geometry of the track and the Čerenkov cone. A track fitting program called YASTEF, developed by the IMB collaboration, has slightly been modified to be used for the Super-Kamiokande detector. The version used for this work, however, is only preliminary. A detailed description of YASTEF can be found elsewhere [24] and is only summarized here.

The fit is found in three phases. In the first phase, a starting point and direction is chosen. Isolated PMT hits are vetoed to reject scattered light. Then the starting values are obtained using a point-fitter.

The starting point is usually near the track axis but not necessarily close to the actual vertex. Therefore, in the second phase the position is mainly adjusted parallel to the track to get a value that is close to the event vertex. In a three step cycle the direction, the position along the track and the position perpendicular to the track are adjusted. The direction is found by maximizing the charge inside a cone. An angular charge distribution is

histogramed about the trial direction. The sharpest point of that histogram is identified as the edge of the Čerenkov ring. Then the vertex position is adjusted along the track to form a cone with the correct Čerenkov angle. The vertex is then moved perpendicular to the track to minimize the residual.

The final phase improves the fit using a similar procedure as the above. In this case, however, the direction and the position perpendicular to the track are adjusted by maximizing the "sharpness" of the ring, which is defined as the maximum derivative of the angular charge distribution mentioned above.

The performance of YASTEF has been analyzed with samples of monoenergetic Monte Carlo events. In Figure 4.3 the difference between the true and the fitted position parallel and perpendicular to the track are histogramed. The fitted position along the track is systematically shifted backwards for electrons and forwards for muons. This is due to the difference in angular charge distribution and can only be corrected knowing the identity of the particle.

4.3 Particle Identification

As discussed in Section 2.3, the best suited quantity to test our understanding of production and propagation of neutrinos, including new neutrino

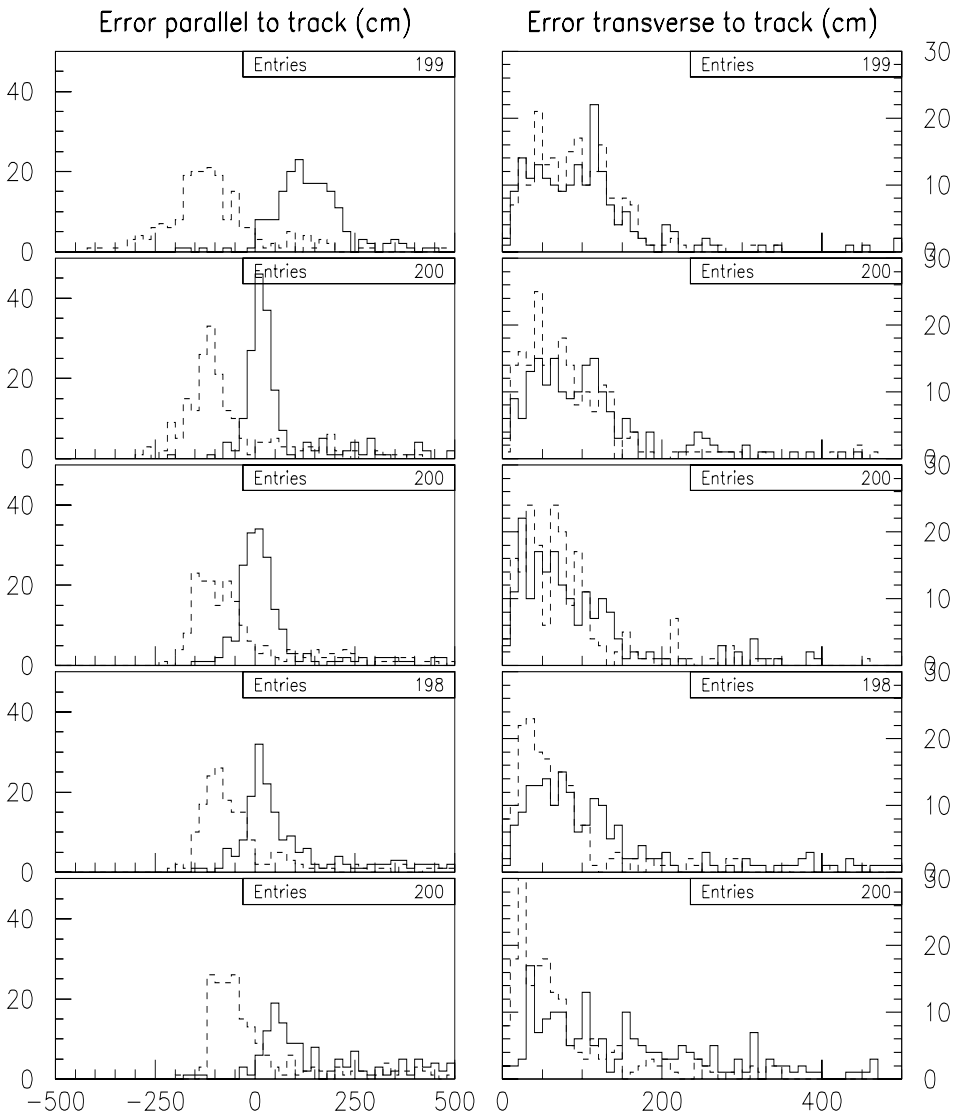

Figure 4.3: The position resolution of YASTEF parallel to the track (left column) and perpendicular to the track (right column). Dotted lines are Monte Carlo electrons, solid lines are MC muons. The energies from top to bottom row are: electrons: 100 MeV, 300 MeV, 600 MeV, 1000 MeV, 1800 MeV; muons: 300 MeV, 500 MeV, 800 MeV, 1200 MeV, 2000 MeV.

physics, is the ratio $(\nu_\mu + \overline{\nu}_\mu)/(\nu_e + \overline{\nu}_e)$. It is therefore necessary to determine the flavor of the observed neutrinos. In charged current interactions a lepton with the flavor of the original neutrino is produced. For quasi-elastic interactions it is therefore possible to infer the presence of a ν_e by observing the creation of an electron, and a ν_μ by identifying a produced muon (here and in the following anti particles are not mentioned explicitly). The situation is more complicated for inelastic scattering. If the additional pions or their decay products (muons and electrons) are above Čerenkov threshold, they may lead to misinterpretations.

The following describes a method developed to distinguish electron-like Čerenkov rings form muon-like ones. Electron-like refers to massless / showering particles (electrons and photons) and muon-like events to massive / non-showering particles (muon, pions etc.). The Čerenkov PMT hit patterns for muon-type events and electron-type events are qualitatively different. A muon-type event creates a ring pattern with a sharp outer edge whereas an electron creates a ring with a more diffuse edge. The edges correspond to the intersection of the 42^0 Čerenkov cone with the detector. As highly energetic electrons develop electromagnetic showers by bremsstrahlung and pair production, the Čerenkov light actually comes from many short tracks of electrons in the shower. As they slightly spread in direction, the ring pattern is smeared out. Figures 4.4 and 4.5 show hit-patterns of a "typical" electron

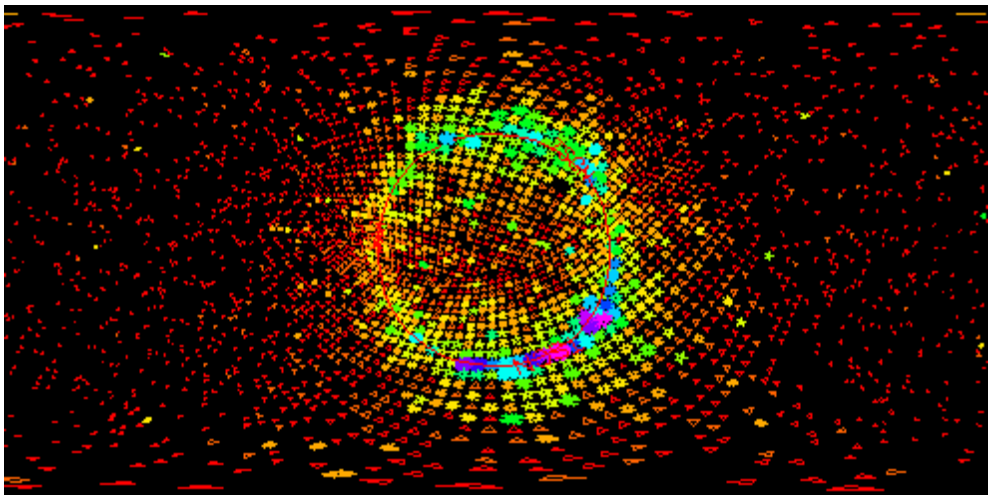

Figure 4.4: Scan of an electron in cylindrical perspective. This perspective shows what can be seen, if the observer is at the vertex point and is facing in direction of the motion of the particle. The grey scale denotes the charge of the PMTs.

and a "typical" muon respectively.

Charge Track Distribution

Particle identification using the hit pattern is in principle a 2-dim pattern recognition problem. A simple mapping, however, can reduce this to a 1-dim problem without losing much information, since the problem is symmetric with respect to rotation around the axis given by the motion of the particle. First, the vertex and direction of the particle are determined. They define a straight line called the trajectory. For each hit PMT, the point where the Čerenkov photon was emitted along this trajectory is calculated. This assumes that all light came from the trajectory and was emitted at a

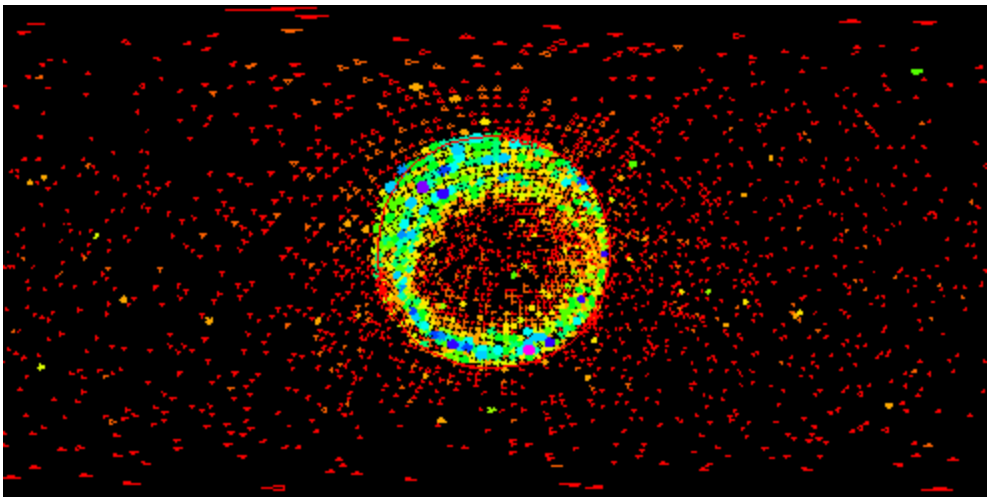

Figure 4.5: Scan of a muon in cylindrical perspective.

42^0 angle. The charge of the PMT (proportional to the amount of light that hit the tube) is then histogramed as a function of the position on the trajectory (see Figure 4.6). This histogram is called charge-track-distribution. Figures 4.7 and 4.8 show the results for the above electron and the muon. It can be seen that in the case of the muon the rising edge of the peak is much steeper. This corresponds to the sharp edge of the muon ring. The particle identification parameter used in this work quantifies the steepness of the peak in the charge-track-distribution.

Particle Identification with RISPID

In the case of an electron, some fraction of the direct Čerenkov light is emitted outside the 42^0 Čerenkov cone. The higher the fraction of photons

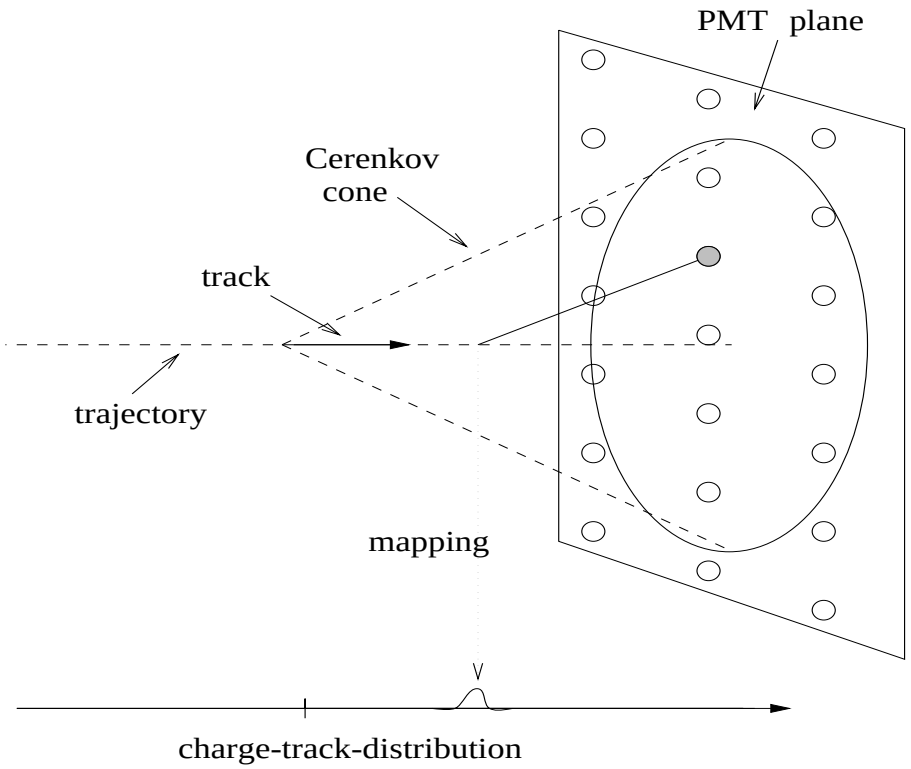

Figure 4.6: Mapping for charge-track-distribution.

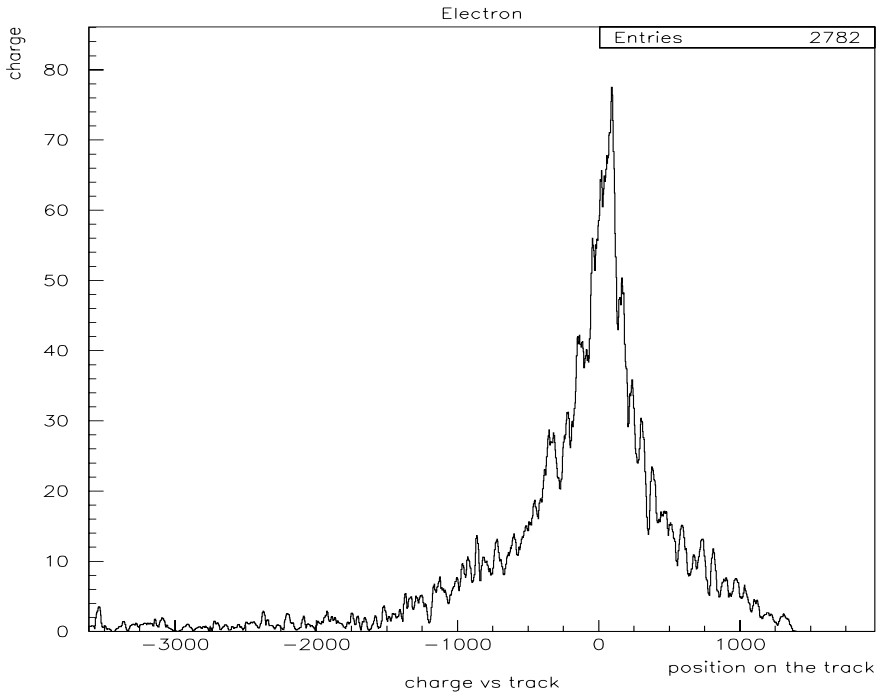

Figure 4.7: Charge-track-distribution for a "typical" electron.

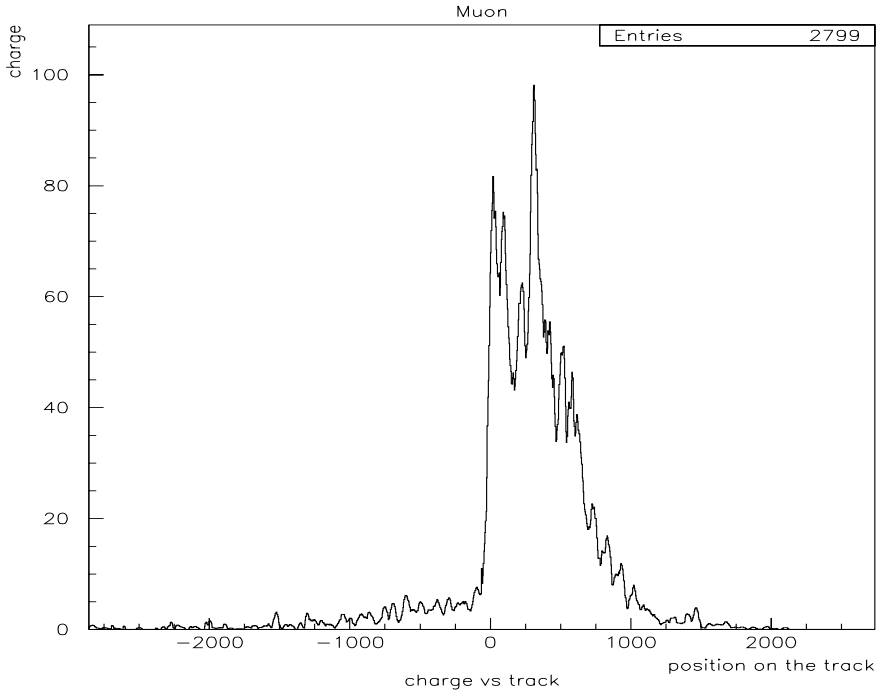

Figure 4.8: Charge-track-distribution for a "typical" muon.

measured outside the cone, the more likely the particle is an electron. To calculate this fraction, the vertex position or a similar well defined value has to be known. The vertex position obtained from YASTEF is not sufficient because its position along the track is systematically different for electrons and muons. The YASTEF fit can, however, be used to histogram a charge-track-distribution. The steepest point in the charge-track-distribution, X_0, can then be used as the event vertex.

The bins of the histogram have to be small enough (2 cm is chosen) to allow sufficiently precise measurement of X_0. This implies that the histogram is not smooth. Particularly, the spacing of the PMTs imposes considerable fluctuations. The numeric derivative $f'(x_i)$ at point x_i is calculated according to:

$$f'(x_i) = \sum_{j=1}^{n} f(x_{i+j}) - f(x_{i-j}) \tag{4.4}$$

where $x_{i+j} - x_i = x_i - x_{i-j}$ is called the width of the mask. A wide mask is insensitive to small scale fluctuations but smears out the details. Therefore, derivatives with two different masks are used (120 cm and 250 cm).

The above definition of X_0 as the steepest point of the peak has to be modified to handle hard scattered muons correctly. Figure 4.9 and 4.10 show the hit pattern and the charge-track-distribution of a hard scattered muon. The maximum derivative might correspond to the inner ring produced by

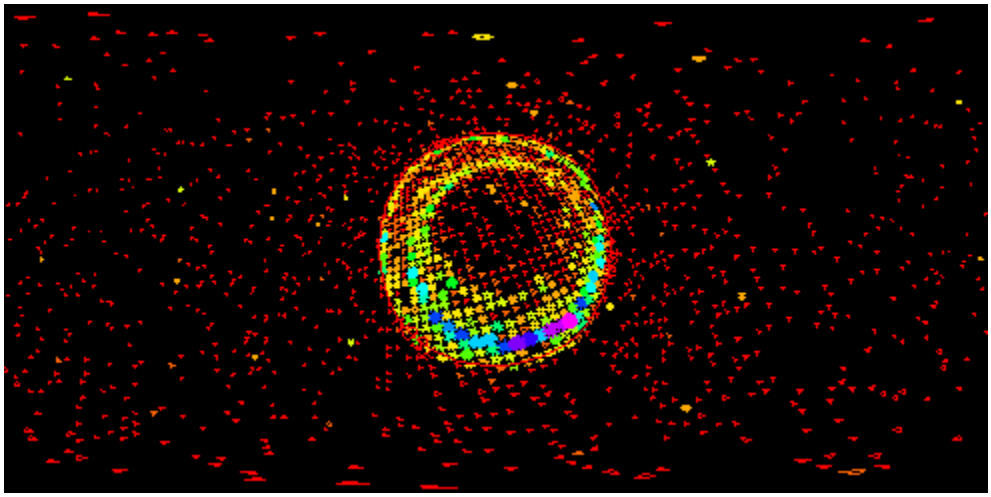

Figure 4.9: Scan of a hard scattered muon in cylindrical perspective.

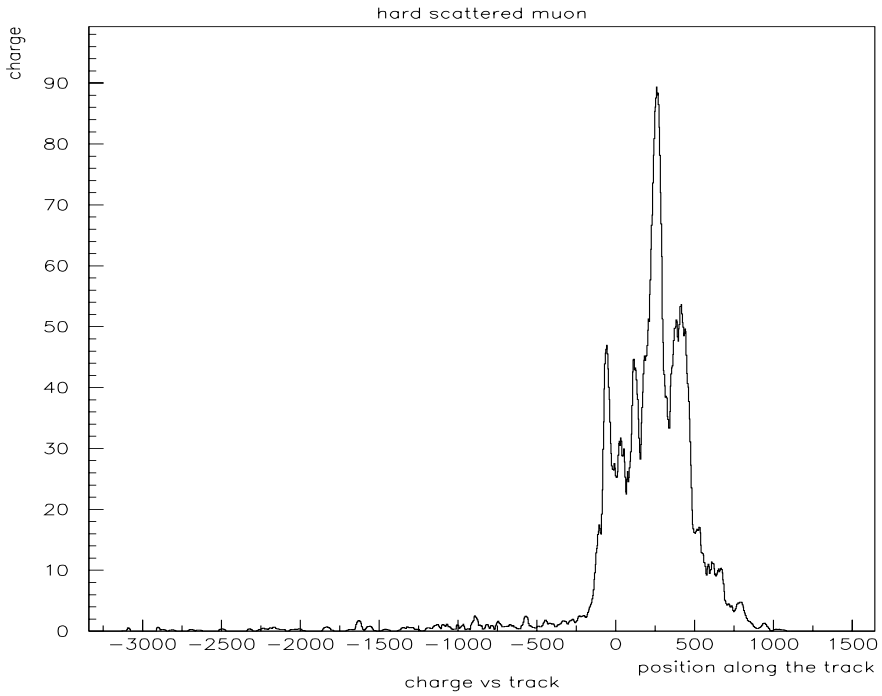

Figure 4.10: Charge-track-distribution of the above hard scattered muon.

the muon after hard scattering. In this case, the outer ring produced before hard scattering is falsely interpreted as smeared out light coming from an electron. Therefore, the outer ring should always be chosen.

Many different procedures have been tested and the following 3 step method has been chosen as the most effective one. Figure 4.11 shows plots of the relevant derivatives for the above "typical" electron.

1. An allowed range for X_0 is determined using the 2nd derivative with wide mask. The range [$x1$,$x2$] is defined by $f''_{wide}(x2)$ = absolute minimum and $f''_{wide}(x1)$ = maximum with $x1 < x2$. This is a protection against distant humps. In the following two steps only values with $x \in [x1, x2]$ are considered.

2. The maximum of the 1st derivative with fine mask, f'^{max}_{fine}, is determined. Then the position $x3$ of the first peak (meaning: x3 as small as possible) with $f'_{fine}(x3) > \frac{1}{2} f'^{max}_{fine}$ is found. This is used because in the case of a hard scattered muon the global maximum might belong to an inner ring.

3. Finally the zero point $f''_{fine}(X_0) = 0$, crossing the x-axis from + to - and lying closest to x3 is determined. This adjustment is done because the zero point of the 2nd derivative can be determined more accurately than the corresponding maximum of the first derivative.

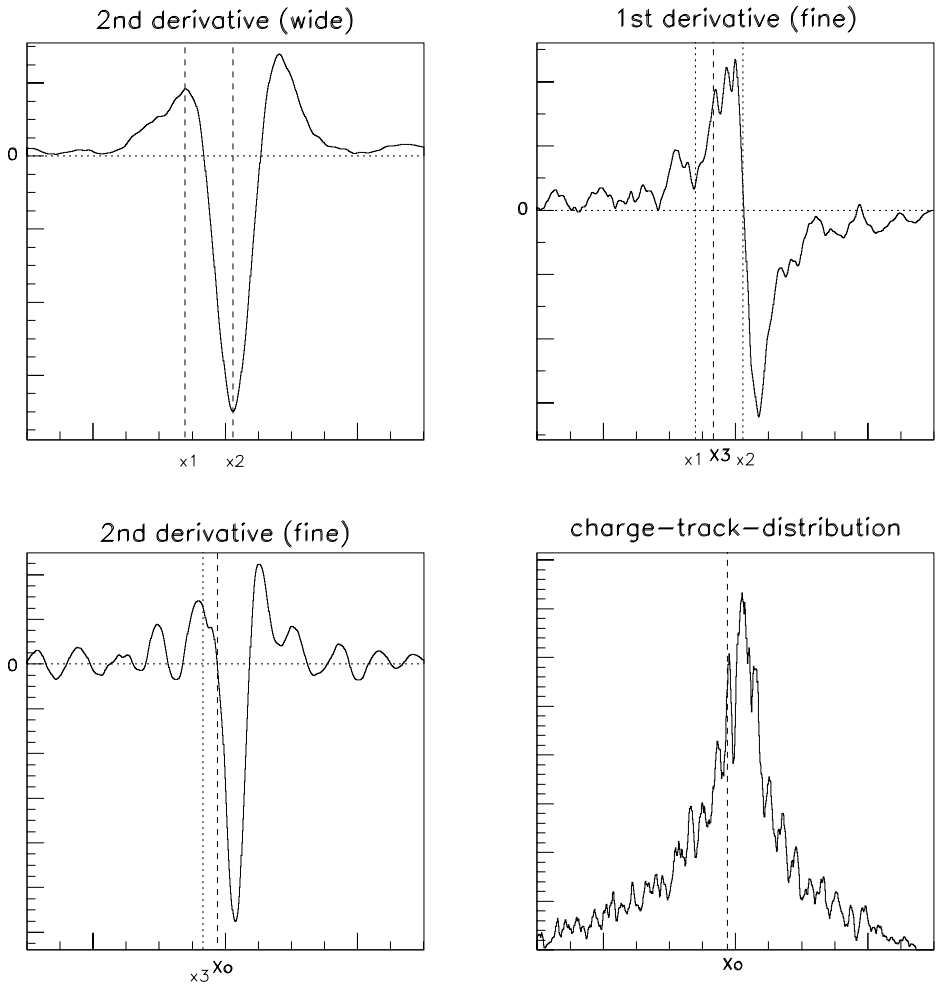

Figure 4.11: The relevant derivatives of the charge-track-distribution of an electron. The values determined by Rispid are shown

Once X_0 is determined, the ratio of the charge integrated 5 meters before and 5 meters after X_0 is calculated. This ratio is called "Rispid" (RISing edge Particle IDentification). If the distance d between X_0 and the intersection of the trajectory with the detector is shorter than 2 meters, Rispid returns an error. If d is between 2 meters and 5 meters, the charge on both sides of X_0 is only integrated over the range given by d.

$$Rispid \equiv \frac{\int_{X_0-\delta}^{X_0} charge}{\int_{X_0}^{X_0+\delta} charge} \qquad \delta = \begin{cases} 5m & \text{if } d \geq 5\text{m} \\ d & \text{if } 5\text{m} > d \geq 2\text{m} \end{cases} \tag{4.5}$$

The Rispid value for a sample of 300 MeV MC electrons and 500 MeV MC muons is shown in Figure 4.12. The vertex point and direction were determined using YASTEF. In this sample 91.1% of the muons have a Rispid value smaller than 0.22 and 92.4% of the electrons have a value greater than 0.22. For the samples in Figure 4.12 a fiducial cut is applied which requires the vertex to be at least 2 meters inside the inner walls (this requirement is more strict than the "2 m along the track" cut mentioned above). This cut is motivated by Figure 4.13 which shows the distribution of Rispid as a function of the distance to the wall of the inner detector.

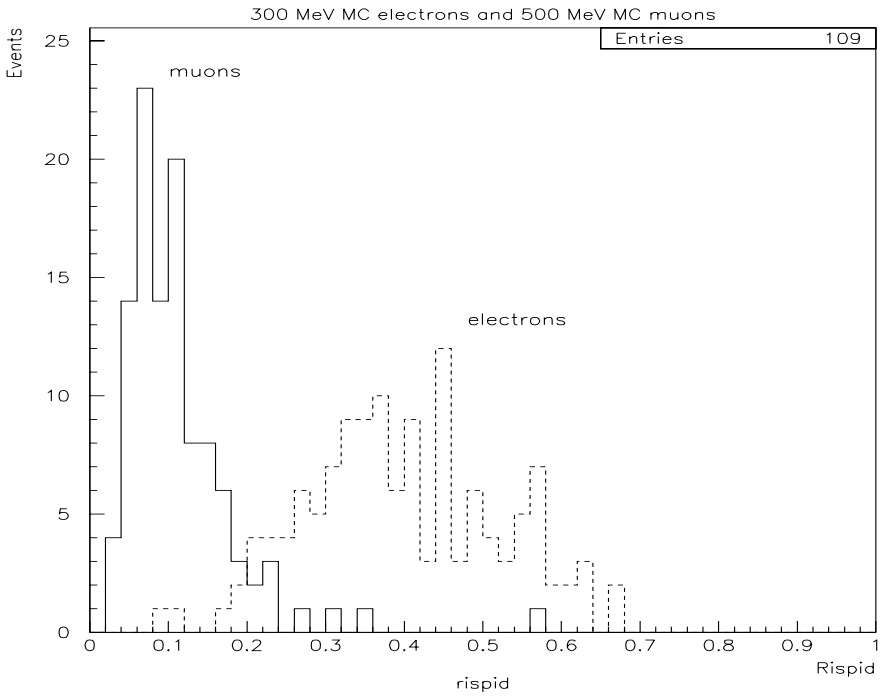

Figure 4.12: Rispid value for 300 MeV MC electrons and 500 MeV MC muons. The difference in energy for electrons and muons is chosen so that the events in both samples have similar charge (radiated Čerenkov light).

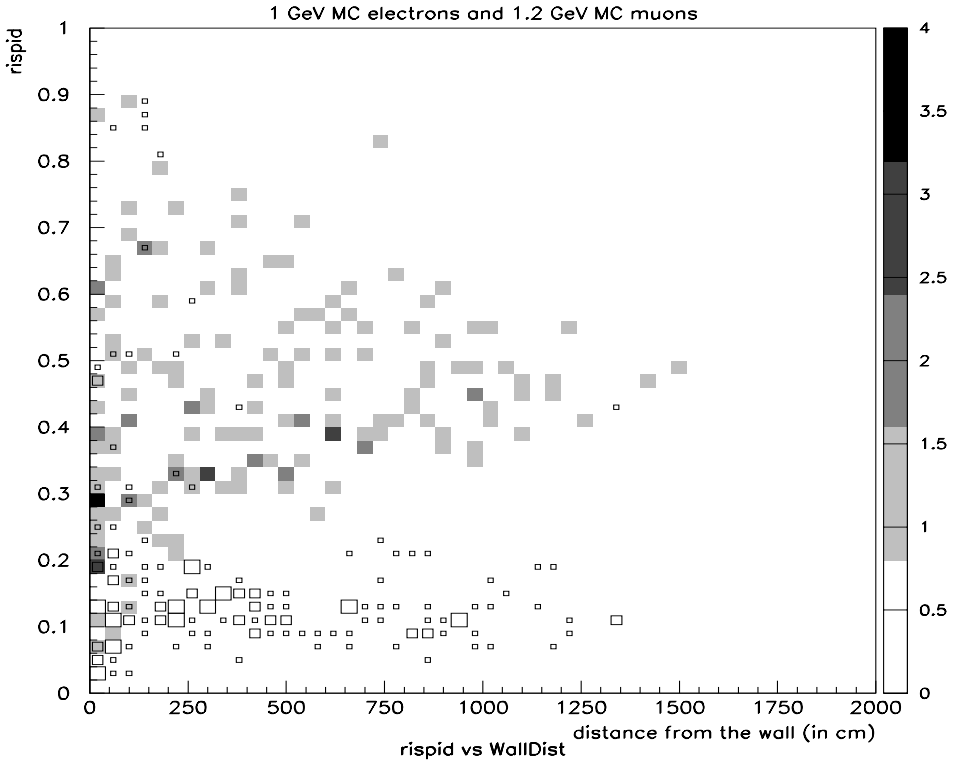

Figure 4.13: Rispid as function of the distance to the wall of the inner detector. Shaded boxes: 1 GeV electrons; open boxes: 1.2 GeV muons. The separation is bad for distances smaller than 200 cm.

Rispid-Grid

The "raw" Rispid value in many cases is not very useful. There are two reasons for that. First, the fitted vertex might not be very accurate. However, even with an exact (e.g. Monte Carlo) fit the charge-track-distribution of a muon might look like that of an electron, if the muon had a hard-scatter. The shape of the charge-track-distribution is very sensitive to the direction of the track. Figure 4.14 shows the dependence of Rispid on the direction of the fit.

An electron, even using a bad direction, never looks like a muon. Therefore a search for the direction with the most muon-like Rispid value gives much better results than the raw Rispid function. The program "Rispid-grid" calculates Rispid for many directions in a small region around the fitted direction, similar to Figure 4.14. It covers a cone of half opening angle $\cos\Theta = 0.075$ and returns the smallest Rispid value.

In Figure 4.15 the Rispid-grid distribution is shown for the same samples as in Figure 4.12. 97.7% of the electrons have a Rispid value greater than 1.3 and 95.5% of the muons have a value smaller than 1.3. Figure 4.16 displays the Rispid and Rispid-grid distributions for simulated monoenergetic muon and electron samples at 5 different energies. The energy of the muons is chosen to be 200 MeV higher than the energy of the corresponding electrons to obtain pairs of samples with similar "visible energy". The visible energy

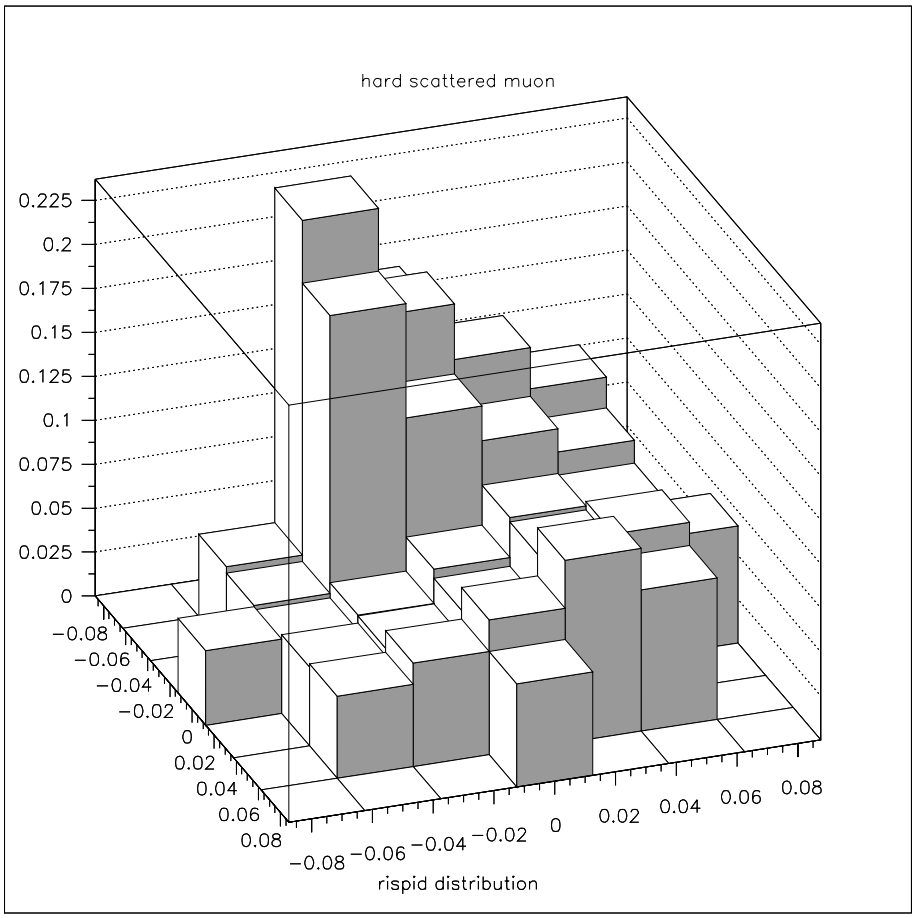

Figure 4.14: Rispid of a hard scattered muon as a function of direction. Using the same vertex position, Rispid is calculated for different directions around the original fitted direction. X and Y denote the cos with respect to the original direction.

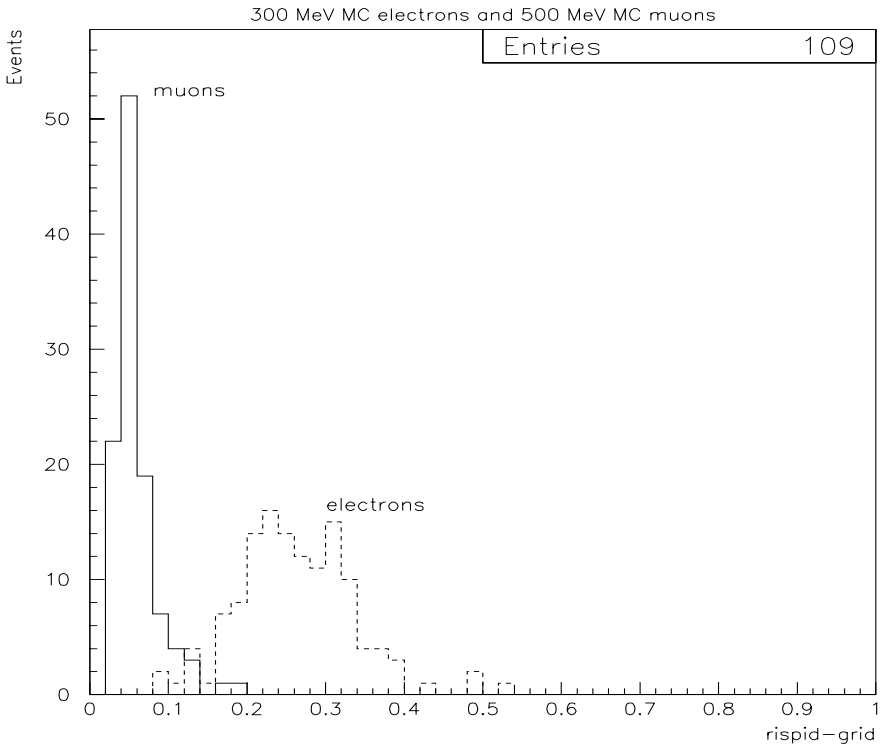

Figure 4.15: Rispid-grid value for 300 MeV MC electrons and 500 MeV MC muons.

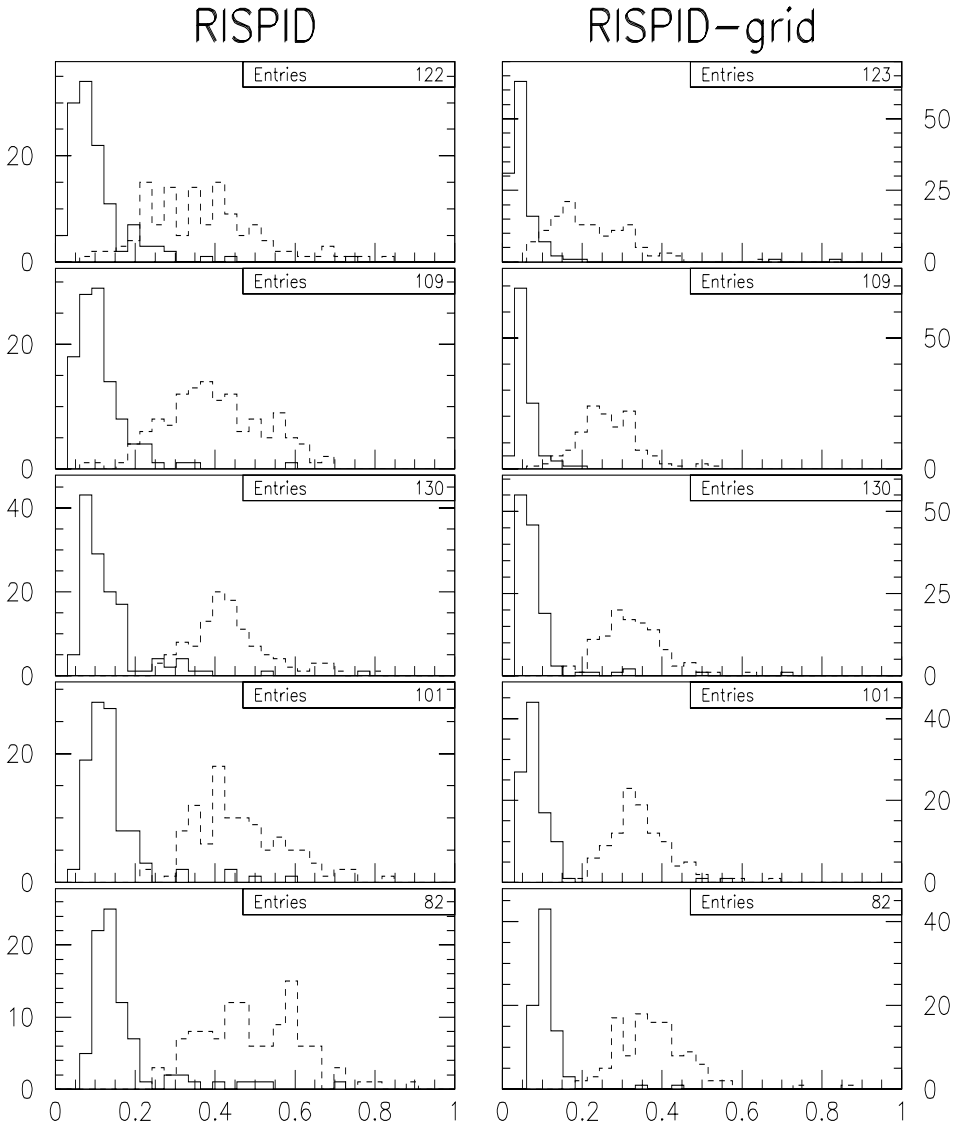

Figure 4.16: Rispid and Rispid-grid for monoenergetic MC muons and electrons. Dotted lines are electrons, solid lines are muons. The energies from top to bottom row are: electrons: 100 MeV, 300 MeV, 600 MeV, 1000 MeV, 1800 MeV; muons: 300 MeV, 500 MeV, 800 MeV, 1200 MeV, 2000 MeV.

Visible Energy in MeV	Rispid-grid cut value	fraction of correctly identified	
		electrons	muons
100	0.1	(93.7±2.2)%	(91.1±2.6)%
300	0.13	(97.7±1.3)%	(95.5±2.0)%
600	0.17	(99.9±0.9)%	(94.6±2.0)%
1000	0.18	(99.1±0.9)%	(96.1±1.9)%
1800	0.2	(100±0.9)%	(97.6±1.7)%

Table 4.1: Rispid-grid identification probability for various energies.

is proportional to the emitted Čerenkov light and for electrons identical to the physical energy.

For each visible energy range a cut value is determined. The fraction of correctly identified muons and electrons are shown in Table 4.1. The errors quoted in this table are statistical errors from a binomial distribution.

Most muons with very large Rispid-values (> 0.2) have a totally wrong YASTEF fits as verified by scanning. The identification efficiency for muons can therefore be improved by hand scanning the fitted vertex point and direction.

Adpid

The energy dependence of Rispid-grid is shown in Figure 4.17. It can be

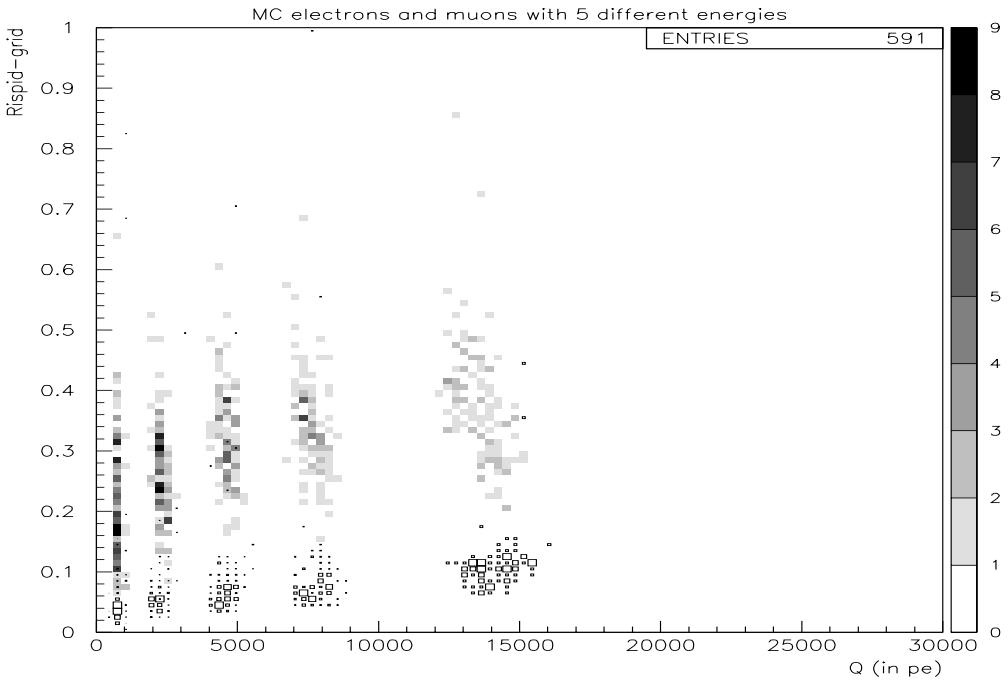

Figure 4.17: The Rispid-grid value of MC samples with different energies are plotted as a function of collected charge. Shaded boxes: electrons; open boxes: muons

seen that the separation value between muons and electrons, R_s, increases with energy. It is desirable to find a parameter that allows an energy independent particle identification. This is essential when Rispid-grid is histogramed for non monoenergetic event samples. An ADjusted risPID-grid value is defined by:

$$Adpid \equiv \frac{Rispid\_grid - R_s(Q)}{Rispid\_grid + R_s(Q)} \tag{4.6}$$

This function is chosen because it maps muon-like values (Rispid-grid $\in$ $[0,R_S(Q)]$) onto [-1,0] and electron-like values (Rispid-grid $\in [R_S(Q),\infty]$) onto [0,1]. To determine $R_S(Q)$ as a function of charge, R_S is first determined as a function of visible energy using the 5 pairs of monoenergetic Monte Carlo samples shown in Figure 4.16. R_S is chosen as the cuts in Table 4.1. Visible energy then has to be converted into units of charge. In this work the charge is given in units that convert the original charge unit (pC) into the equivalent number of photoelectrons (pe). Figure 4.18 shows the charge distribution for the above samples. This plot allows a charge to energy mapping by determining the mean charge-value for each energy. The R_S value for the 5 sample pairs are finally plotted as a function of charge and fitted by straight lines (Figure 4.19). As the resulting function has been determined using Monte Carlo samples, it might need to be modified once an exact energy calibration of the detector has been achieved.

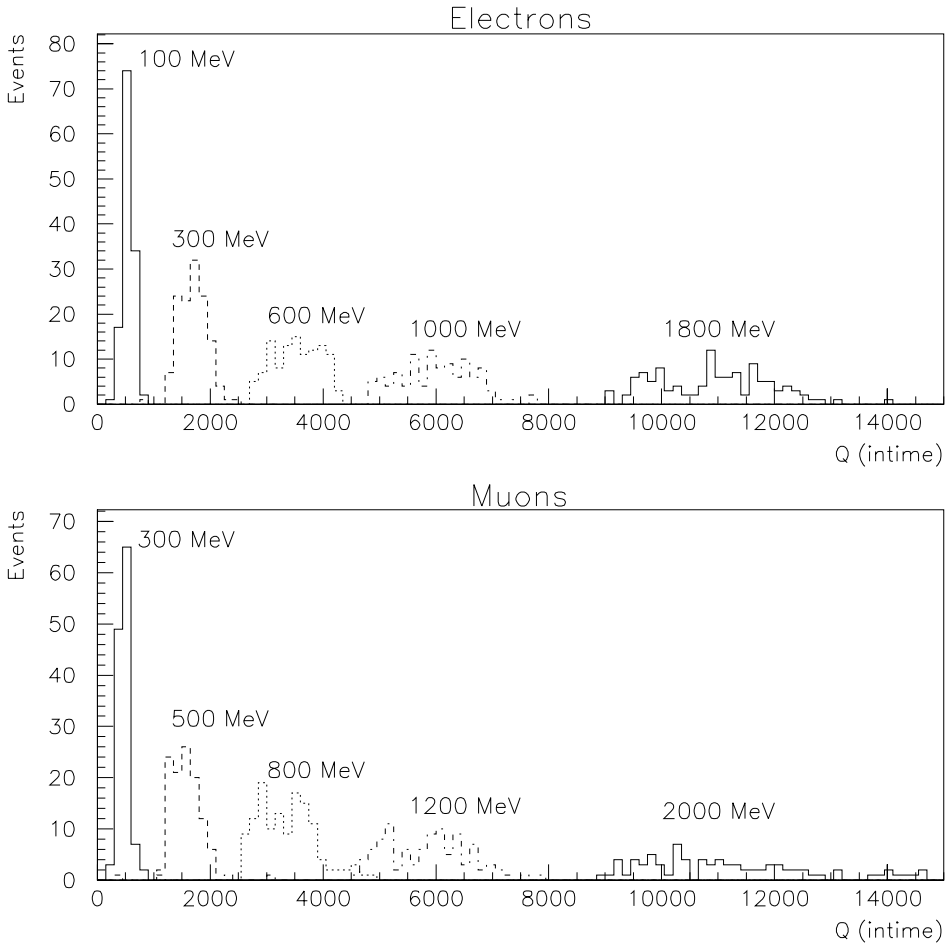

Figure 4.18: The distribution of collected charge for simulated monoenergetic electrons and muons

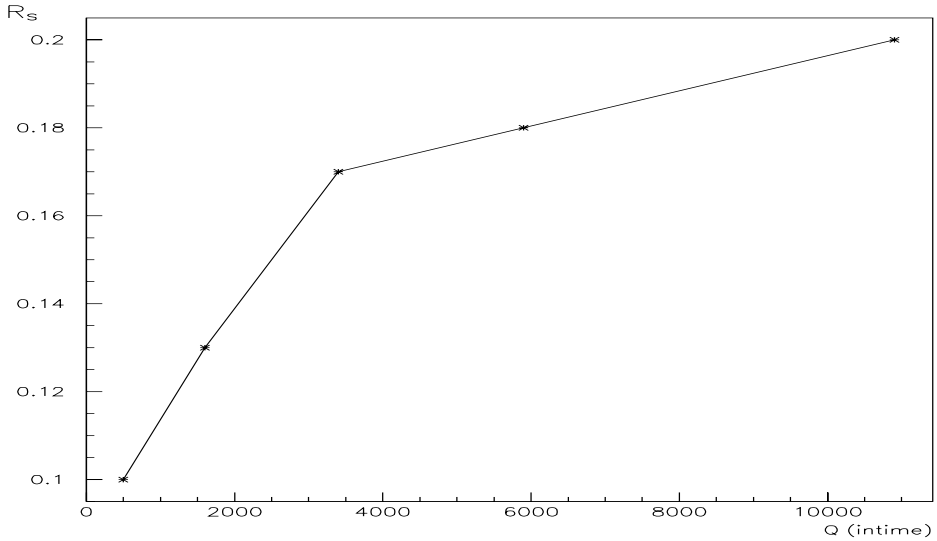

Figure 4.19: The value of Rispid-grid that separates electrons from muons, R_s as a function of collected charge, Q.

Figure 4.20 shows the Adpid value for the samples from Figure 4.17. As expected, muons and electrons are separated by an Adpid value of zero, independent of their energy.

4.4 Event Selection

Before atmospheric neutrino events can be analyzed with the tools described in the previous sections, a sample of candidate events has to be selected out of the flood of events recorded by Super-Kamiokande. The expected $\sim$7 events/day must be filtered out of a data stream with an event rate of about 10 Hz. The efficiency to save atmospheric neutrino events should

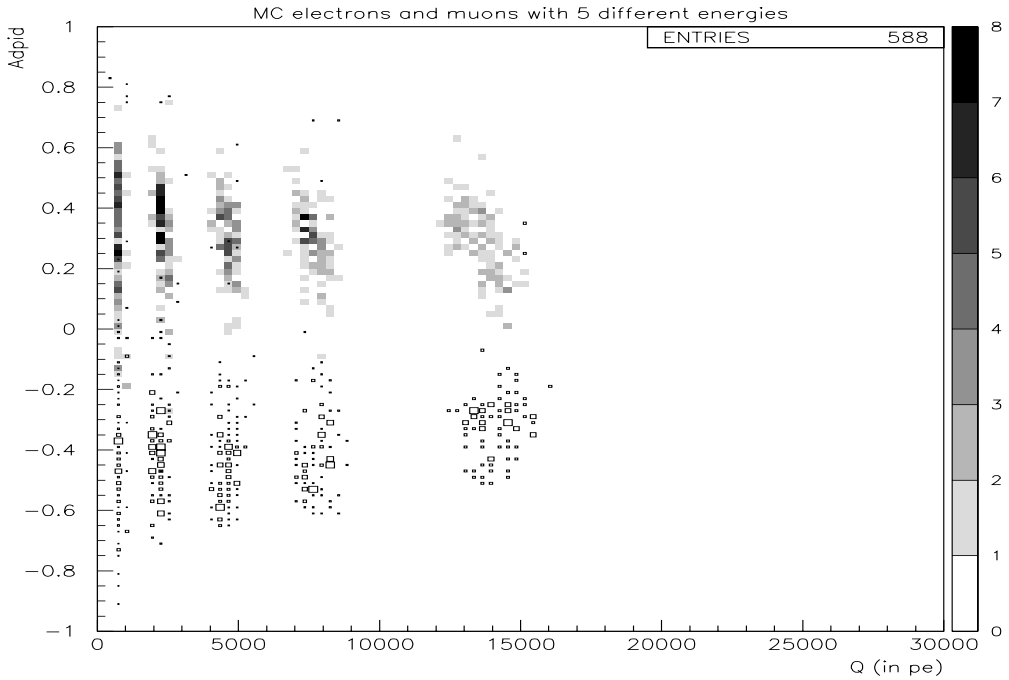

Figure 4.20: The Adpid values of the MC samples from Fig 4.17 are plotted as a function of collected charge. Shaded boxes: electrons; open boxes: muons

be close to 100%, while the data size reduction is maximized.

For the purpose of high energy analysis (atmospheric neutrinos and proton decay as opposed to solar and supernova neutrinos) most events can be rejected by a simple cut on the total light collected. This removes events originating from radon β-decay, nuclear spallations caused by cosmic ray muons, low energy ν-interactions and most kinds of electronic noise.

Entering events like through going and stopping cosmic ray muons are identified by activity in the outer detector. However, to avoid rejection of partially contained events (e.g. muons coming from ν interactions in the inner detector), the outer detector activity has to be confirmed by an inner detector fit. Upward going muons are interesting because they originate from ν interactions in the rocks under the detector.

One type of noise events, so called flashers, is particularly hard to identify. These events originate from defective PMTs that emit light flashes. The timing and geometrical shape of these events can be very similar to "physics" events and some of them can only be removed by hand scanning the event.

The final stage of the US filtering process has not yet been completed. However, a preliminary event selection process has been developed to test fitting and particle identification programs. The following cuts have been made:

- The total charge in the inner detector is required to be above 1600 pC.

This corresponds to a visible energy between 110 MeV and 150 MeV and removes most noise and low energy events.

- The total number of PMT hit in the outer detector must be less than 300. This and the following cut reject entering and exiting events.
- The number of hit outer detector tubes in any 500 nsec window is required to be less the 20.
- The charge of any individual inner PMT is required to be below 400 pC.
- Not more than 5 PMTs in the inner detector can have more than 300 pC.
- No inner PMT is allowed to have more charge than 1/10 of the total inner detector charge. The last three cuts mainly reject flashers and tracks with a very localized exist or entry spot.

In the final step, contained events are selected by hand scanning. The events are displayed showing a projection of the PMT plane with color indicating charge or timing information. Trained on Monte Carlo events a physicist rejects remaining noise events and events that originate close to the wall.

4.5 Comparison with Data

The particle ID parameter Adpid, described in section 4.3 has been developed using Monte Carlo events of electrons and muons with well known energy and momentum. The crucial test for Adpid is its performance on real data.

A sample of 102 single ring contained events has been selected using the filtering cuts described in Section 4.4. Multi-ring events and events with a "bad" YASTEF fit were rejected by hand scanning. Finally a fiducial cut 2 m inside the inner detector has been applied.

The Adpid value calculated for this sample is shown in Figure 4.21. Two clearly separated peaks can be seen. The peak for negative Adpid values can be identified as muons and the one for positive values as electrons.

Atmospheric neutrino events have been simulated using the Monte Carlo described in Section 4.1. The same selection criteria as for the data sample above have been applied to this sample. The Adpid values for the remaining 128 contained single ring MC events are shown in Figure 4.22.

The shape of the histograms for data and Monte Carlo events are similar. The peaks for data, however, appear to be slightly shifted to negative values. A cut at -0.05 instead of 0.0 seems to be appropriate. A likely reason for this difference is that no energy calibration has been available to tune the

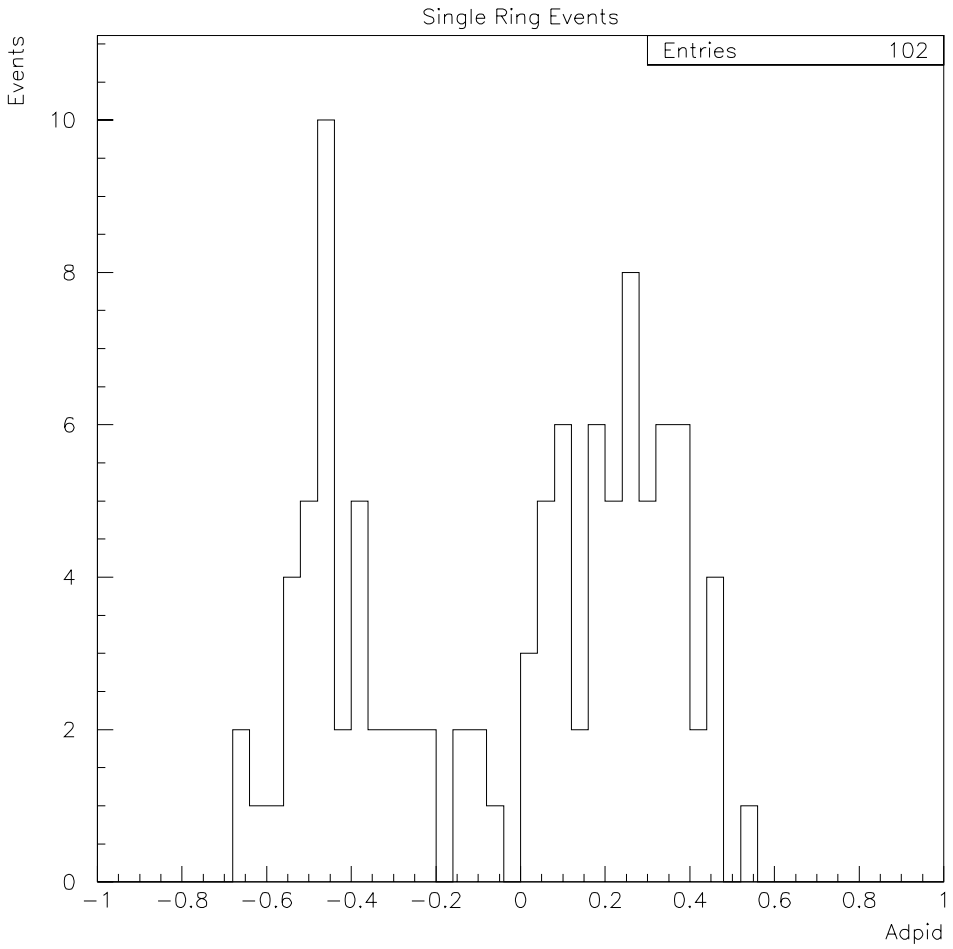

Figure 4.21: Adpid for single ring contained data events

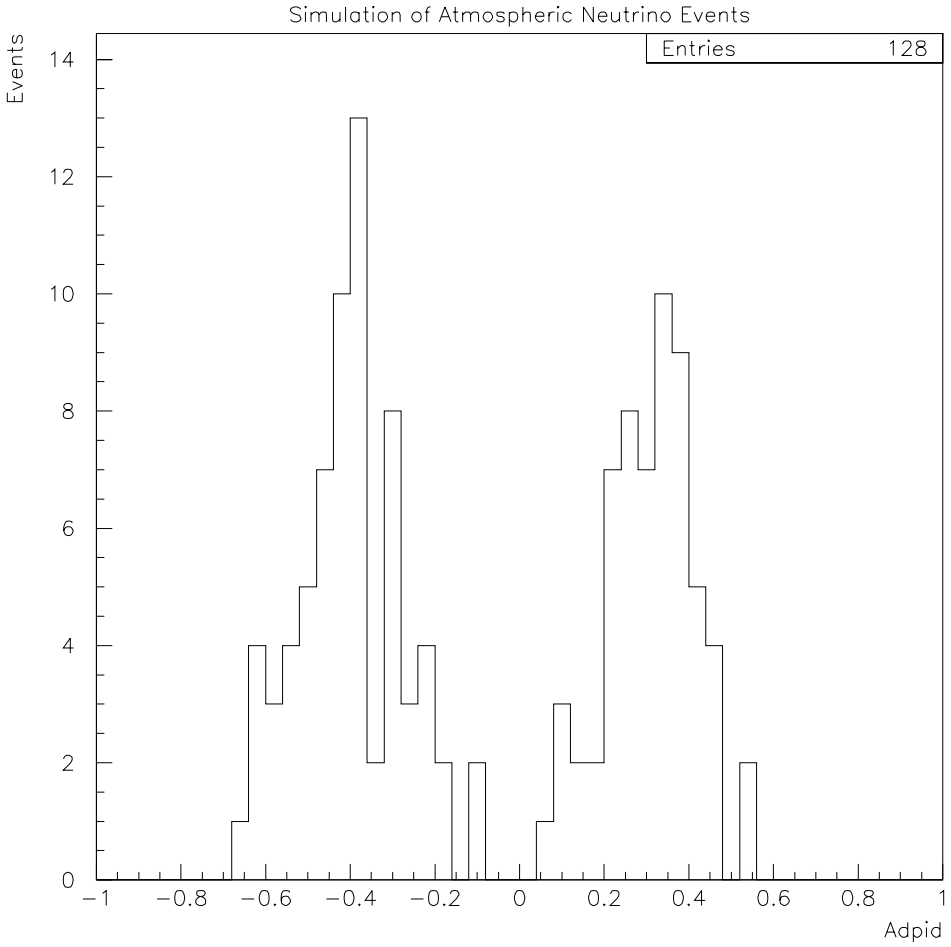

Figure 4.22: Adpid for Monte Carlo single ring contained events

Monte Carlo. The conversion of visible energy to total charge discussed in Section 4.3 probably needs to be corrected.

Muons can also be identified if their decay electron is observed. This can be used to check the performance of Adpid. Out of the above MC and data samples those events are selected that are followed by a decay electron (defined as any event with more than 100 pe total charge in a 1 - 10 μs period after the primary contained event).

Figures 4.23 and 4.24 show that most events of these samples have Adpid values corresponding to the muon peak seen in the previous Figures. However, some events are identified as electrons ($(9.6 \pm 4.1)\%$ for MC; $(19 \pm 7.7)\%$ for data (statistical error only)). Hand scanning of these events shows that most of them actually look like "typical" electrons. Indeed, one expects to find some contained electron events that are followed by a decay electron event. In inelastic interactions pions below Čerenkov threshold can be created in addition to an electron. These pions decay into muons whose decay electrons can be detected.

4.6 Conclusion

An algorithm for particle identification of atmospheric neutrinos with the Super-Kamiokande detector has been developed. The efficiency to correctly

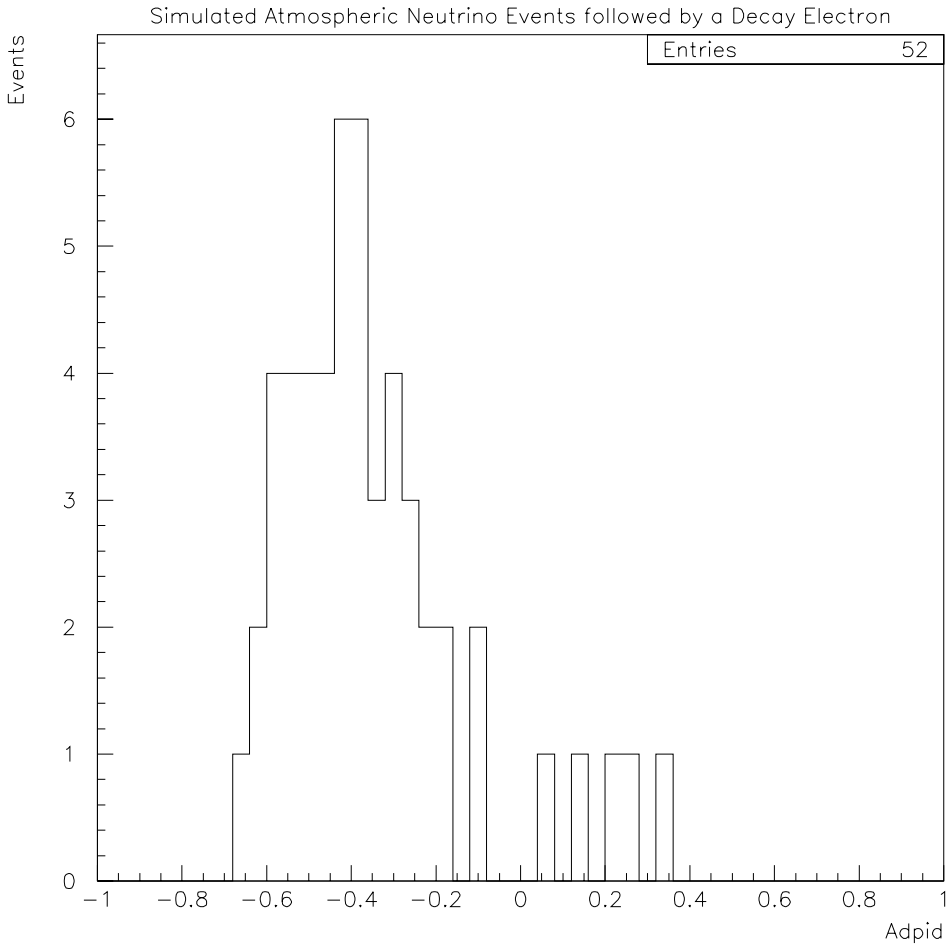

Figure 4.23: Adpid for Monte Carlo single ring contained events that are followed by a decay electron

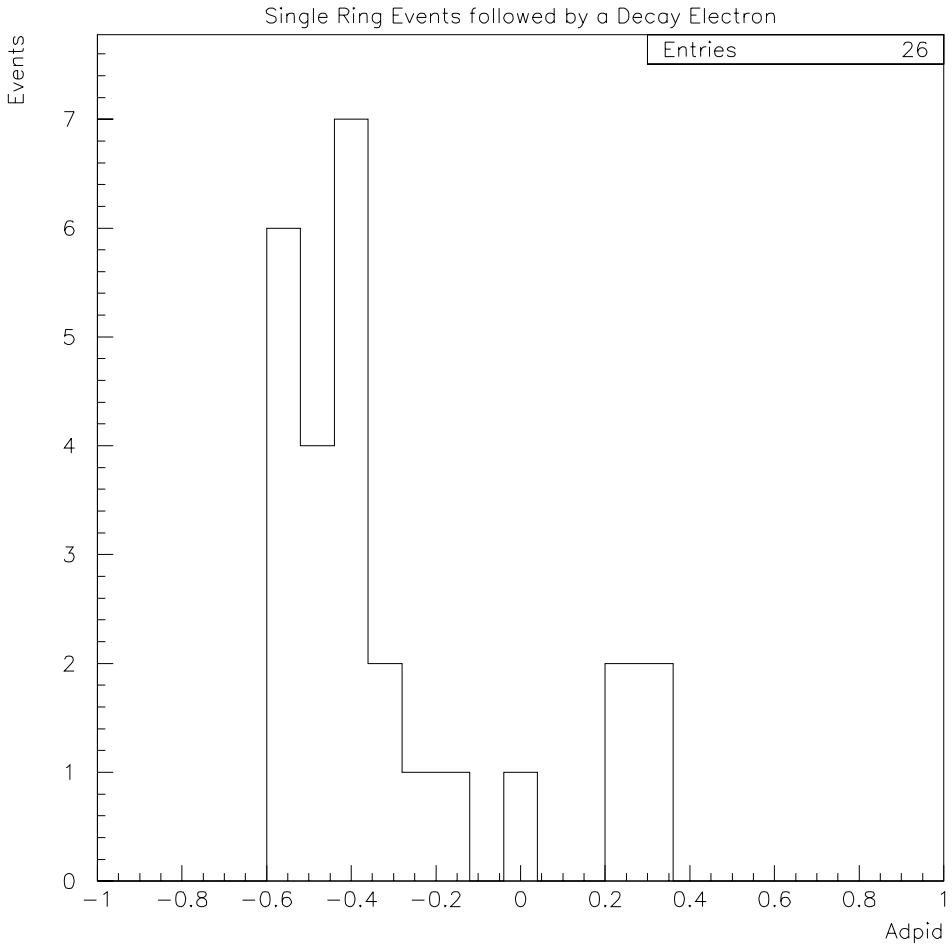

Figure 4.24: Adpid for single ring contained data events that are followed by a decay electron

identify Monte Carlo particles with 100 MeV visible energy is $(93.7 \pm 2.2)\%$ for electrons and $(91.1 \pm 2.6)\%$ for muons (the uncertainty represents only a statistical error). The identification efficiency increases with the energy of the particle ($(99.1 \pm 0.9)\%$ for electrons and $(96.1 \pm 1.9)\%$ for muons at 1 GeV visible energy). A preliminary study on a data sample of μ-decay candidates shows that the misidentification probability is smaller than 20%.

The work presented in this thesis is preliminary in many ways. The Monte Carlo simulation program used to develop the particle identification algorithm Adpid has not yet been completely tuned and compared to data. Particularly, the particle ID program is sensitive to correct energy calibration and light scattering parameters. A more reliable fitter than the one used in this work is being developed and will most likely improve the performance of Adpid.

Bibliography

[1] B. Kayser, *with* F. Gibrat-Debu and F. Perrier, *The Physics of Massive Neutrinos* , (World Scientific Publishing Co. Pte. Ltd., Teaneck, N.J., 1989)

[2] C.B. Bratton et al., *Proposal to Participate in the Super-Kamiokande Project*, (Proposal submitted to and approved by DoE 1992)

[3] Takaaki Kajita, *Observation of Atmospheric Neutrinos*, (Physics and Astrophysics of Neutrinos, p559, Springer-Verlag 1994)

[4] J.N. Bahcall and R.K. Ulrich, *Solar Models, Neutrino Experiments, and Helioseismology*, (Rev. Mod. Phys. **60**, 297 (1988))

[5] G. Battistoni et al., *The NUSEX Detector*, (Nucl. Inst. Meth **A245**, 277 (1986))

[6] Ch. Berger et al., *The Frejus Nucleon Decay Detector*, (Nucl. Inst. Meth **A262**, 463 (1987))

[7] D. W. Casper *Experimental Neutrino Physics and Astrophysics with the IMB-3 Detector*, (Doctoral Dissertation, University of Michigan, 1990)

[8] M. Takita *An Experimental Study of the Atmospheric Neutrino Flux with the Kamiokande Detector*, (Doctoral Dissertation, University of Tokyo, 1988)

[9] W. Pauli, Proc. VII Solvay Congress, Brussels (Paris: Gauthier-Villars, 1933), 324.

[10] D. Griffiths, *Introduction to Elementary Particle Physics*, (Wiley & Sons, New York, 1987)

[11] F. Reines and C.L. Cowan Jr., *Detection of free Neutrino*, (Phys. Rev. **92**, 830 (1953))

[12] L. Montanet et al., (Particle Data Group), Phys. Rev. **D**50, 1173 (1994). (the **Particle Data Book**)

[13] Pontecorvo, B., *Zh. Eksp. Theor. Phys.* **33**, 549 1957, translated *Sov. Phys. JETP* **6**, 429 (1958).

[14] L. Wolfenstein, *Neutrino oscillations in matter*, (Phys. Rev. D **17**, 2369 (1978))

[15] M. Honda, T. Kajita, K. Kasahara and S. Midorikawa, *Calculation of Flux of Atmospheric Neutrinos*, (Phys. Rev. D **52**, 4985 (1995))

[16] G. Barr, T.K. Gaisser and T. Stanev, *Flux of Atmospheric Neutrinos*, (Phys. Rev. D **39**, 3532 (1989))

[17] E.V. Bugaev and V.A. Naumov, *On the Interpretation of the Kamiokande Neutrino Experiment*, (Phys. Lett. B **232**, 391 (1989))

[18] H. Lee, Y. S. Koh, *A new Calculation of Atmospheric Neutrino Flux*, (Il Nuovo Cimento, **105B**, 883 (1990))

[19] G.T. Zatsepin and V. A. Kuzmin, *Angular distributions of high-energy muons in the atmosphere and their production mechanism*, (Soviet Physics JEPT, **12**, 1171 (1961))

[20] D. Rein and L.M. Sehgal, *Neutrino-excitation of baryon resonances and single pion production.*, (Ann. Phys. **133**, 79 (1981))

[21] G.L. Fogli and G. Nardulli, *A new Approach to the Charge Current induced weak One-Pion Production*, (Nucl. Phys. **B160**, 116 (1979))

[22] J.D.Jackson, *Classical Electrodynamics*, (Wiley & Sons, New York, 1975)

[23] A. Suzuki et al., *Improvement of 20-inch Diameter Photomultiplier Tubes*, (KEK Preprint 92-50, July 1992)

[24] C. McGrew *A Search for Baryon Non-Conservation using the IMB-3 Detector*, (Doctoral Dissertation, UC Irvine, 1994)